Electronic Supplementary Material (ESI) for Energy & Environmental Science.

Supporting Information

Self-assembled Hierarchical Nanostructured Perovskites Enable Highly Efficient LEDs via Energy Cascade

Xin Yu Chin,[a] Ajay Perumal,[b] Annalisa Bruno,[a] Natalia Yantara,[a] Sjoerd A. Veldhuis,[a] Laura Martínez-Sarti,[c] Bevita Chandran,[d] Vladimir Chirvony,[c] Alencious Shu-Zee Lo,[e] Jinkyu So,[e] Cesare Soci,[e] Michael Grätzel,[f] Henk J. Bolink,[c] Nripan Mathews,*[ad] Subodh G. Mhaisalkar*[ad]

[a] *Energy Research Institute at Nanyang Technological University (ERI@N), 50 Nanyang Drive, Research Techno Plaza, X-Frontier Block, Level 5, Singapore 637553, Singapore.*

[b] *Department of Physics, Indian Institute of Science Education and Research (IISER) Berhampur, Odisha, 760010, India.*

[c] *Instituto de Ciencia Molecular, Universidad de Valencia C/ Cat. J. Beltran 2, 46980 Paterna, Spain.*

[d] *School of Materials Science and Engineering, Nanyang Technological University, 639798 Singapore.*

[e] *Centre of Disruptive Photonics Technologies, Division of Physics and Applied Physics, School of Physical and Mathematical Sciences, Nanyang Technological University, 637371 Singapore.*

[f] *Laboratory of Photonics and Interfaces, Department of Chemistry and Chemical Engineering, Swiss Federal Institute of Technology, Station 6, Lausanne 1015, Switzerland.*

Experimental details

Nanocrystal (NC) synthesis & NC ink formation: Ligand-assisted reprecipitation (LARP) method was used to synthesize the $FAPbBr_3$ nanocrystals at room temperature. Precursor solutions were prepared by mixing 0.2 mmol of FABr (formamidinium bromideDyesol) and 0.1 mmol of $PbBr_2$ (99.999% trace metal basis, Sigma Aldrich) in 0.5 mL of DMF (anhydrous *N,N*-dimethylformamide, 99.8%, Sigma Aldrich). For each synthesis, 150 µL of the prepared 0.5 mL precursor solution was added dropwise into a vigorously stirred solution containing 5 mL toluene, 15-50 µL *n*-octylamine (OA:$PbBr_2$ 3:1 to 10:1; needed to passivate the as-formed NCs and concurrent formation of 2D layered perovskites), 0.3 mL oleic acid, and 2 mL *n*-butanol. Immediately after injection, a yellowish solution was formed, indicating the formation of $FAPbBr_3$ NCs. After reaction completion, the colloidal NC solution was washed using two centrifugation steps. In the first step, the NC solution was centrifuged at 14,680 rpm (g-force ~21,000), after which the supernatant phase was discarded and the precipitate redispersed in 1 mL of toluene. In the second centrifugation step, the redispersed NCs were centrifugated at 3,750 rpm (g-force ~1,300). The resultant supernatant phase was used as NC ink (estimated concentration ~8-10 mg mL^{-1}) for the LED device fabrication. Very similar results were obtained in Valencia when slightly different centrifuge settings were used, namely; 13,400 rpm and 4,400 rpm for the first and second step, respectively. It should be noted that a lower quantity of octylamine (< 15 µL) yield a much lower concentration of NC, since octylamiene is also a ligand component of NC to achieve colloidal suspension properties. The entire synthetic protocol is conducted in a fume hood under ambient conditions, whereas the thin film formation (i.e. spin-coating of the NC ink) was performed under inert atmosphere (Ar or N_2; with H_2O and O_2 levels <0.1 ppm). Noted that the entire synthesis procedure is conducted in chemical fumehood, while the spincoating of the NC ink is performed in an inert atmospheric glovebox.

Device fabrication: Pre-etched indium-tin oxide (ITO; sheet resistance ~8 Ω cm^{-1}; Wuhan Jinge Solar Energy Technology Co., Ltd) glass substrates were used as-purchased, and sequentially washed in detergent solution, acetone, ethanol, and 2-propanol in an ultrasonication bath. Subsequently, the substrates were dried and treated for 20 min with UV-ozone. The hole transporting layer, PEDOT:PSS (Clevios 4083; filtered with 0.45 µm PVDF filter) was then spin-coated for 1 min at 4000 rpm and thermally annealed for 10 min at 130 °C to remove any residual solvent. The substrates were transferred into an argon-filled glovebox for the spin-coating of active emission materials. The NC inks (20 µL of NC ink was used per square centimeter of substrate area) were dropcasted on top of the PEDOT:PSS layer and left for 5 min to slowly evaporate (and initiate self-assembly), prior to spin-coating for 1 min at 1000 rpm, to obtain thin film of ~40 nm thick (see cross-sectional SEM images, Fig. S12). 45 nm of electron transporting layer (either POT2T, 2,4,6-Tris[3-(diphenylphosphinyl)phenyl]-1,3,5-triazine, or B3PYMPM, 4,6-Bis(3,5-di(pyridin-3-yl)phenyl)-2-methylpyrimidine) is thermally evaporated under high vacuum (10^{-6} torr). Lastly, the cathode materials Ca (7 nm) and Al (80 nm) were subsequently thermally evaporated through a metal shadow mask, to define the device active area of 3 mm^2. Flexible devices (with active area 3 mm^2) were fabricated on ITO/PET substrates following a similar protocol, although thicker PEDOT:PSS layers (ca. 80 nm) were deposited. A filtered PEDOT:PSS solution was spin-coated at 1000 rpm for 60 s, followed by thermal annealing at 120 °C for 10 min to reduce the surface roughness (i.e. due to the rough ITO layer on the flexible PET substrate). The ITO/PET substrates were etched with Zn powder and diluted hydrochloric acid, and subsequent sonication in soap water, acetone, ethanol, and 2-propanol for 10 min. The deposition of subsequent emissive layer, electron transporting layer, and cathode were the same as the standard devices fabricated on ITO/glass substrates. Large area devices are prepared similarly to the standard 3 mm^2 devices fabricated on ITO/glass substrates.

LED device characterization: All LED devices were encapsulated with epoxy resin before taken out from argon-filled glovebox for electroluminescence characterization. A Keithley 2612B was used to obtain the current-voltage characteristics of the LED devices using a scan rate of 1 V s^{-1} (step size 0.1 V, step interval 0.1 s), unless stated otherwise. The light emission was collected by an integrating sphere (OceanOptics FOIS-1) coupled to a calibrated spectrophotometer (OceanOptics QEPro). An OceanOptics HL-3 Plus vis-NIR light source, calibrated using a procedure and documentation patterned after the ISO 17025, IEC Guide 115 and JCGM100:2008 (GUM) protocols, is used to calibrate the absolute irradiance measurement of the spectrometer. As LED devices are placed on outside of the integrating sphere, only forward emission is captured while the edge emission contribution is loss outside the integrating sphere. This method has also been widely used to measure the external quantum efficiency of organic light emitting diode.[1, 2] A schematic of the experimental setup is available in Fig. S25.

LED device stability: Before the stability test, the current-voltage-luminance characteristics of each device was recorded by sweeping voltages up to 2.9 V only to minimize the bias-stress degradation on the device. A constant current density was applied according to the current-voltage-luminance characteristics. For initial luminance L_0 ~100 cd m^{-2}, the luminance of the device decayed to half of the initial luminance after ~800 s (approx. 13 min).

X-ray diffraction: The crystal phase and lattice parameters of the thin films of synthesized NCs were determined using a Bruker D8 advance diffractometer with a 0D LynxEYE™ detector. Scans from 2θ = 5-35° were recorded (step sizes of 0.05° and 10 s per step) of thin films spin-coated on cleaned glass substrates coated with PEDOT:PSS (see device fabrication protocol). Rocking curves of the (001) and (002) reflections of 2D $(OA)_2(FA)_{n-1}Pb_nBr_{3n+1}$ (2θ ~9.6°) and 3D $FAPbBr_3$ (2θ ~29.8°) were recorded from ω = 2-6° and ω = 13-17°, respectively, with step sizes of 0.05° and 10 s per step.

Scanning transmission electron microscopy: Measurements were performed with a Tecnai G2 F20 with a Schottky field emitter operated at 200kV. Selected samples were diluted in toluene, dropcasted on a carbon-copper grid, and mounted on a FEI Double Tilt Analytical Holder for examination. Tecnai G2 F20 STEM with an X-Twin lens objective lenses and field emission gun (Schottky field emitter) operates at a beam current of > 100 nA, providing high probe current (0.5 nA or more in 1 nm probe). The system is equipped with a fully embedded digital scan system; bright-field and annular dark-field modes are provided by ultra-high resolution high-angle annular dark-field (HAADF) detector.

Field-emission scanning electron microscopy: The morphological images of the films were recorded using field-emission scanning electron microscope (FE-SEM, JEOL, J7600F).

Cathodoluminescence microscopy: The measurements were performed in a scanning electron microscope equipped with a cathodoluminescence detection system, Attolight CL Allalin 4027 Chronos. A focused electron beam (electron energy 5 keV; beam current ~11 nA; dwell time 10-200 ms) scanned the samples while recording the light emission spectrum synchronously to produce hyperspectral images. The emitted light was collected by an achromatic reflective objective with a high numerical aperture (NA = 0.72) and sent to a UV-VIS spectrometer (Horiba iHR320) equipped with a thermoelectrically cooled silicon CCD array (Andor Newton).

Small angle x-ray scattering: The Xenocs Nano-inXider, equipped with a Dectris Pilatus3 hybrid pixel detector was employed to record the combined small- and wide-angle X-ray scattering (SAXS/WAXS) patterns of NC inks. This allowed to measure an effective scattering vector magnitude in the range of $0.1 < q < 4$ nm^{-1} in SAXS, and up to 2θ = 60° in WAXS. NC inks with OA:$PbBr_2$ ratios 3:1, 4:1, 5:1, 7:1, and 10:1 were measured in sealed glass capillaries (inner diameter 0.95 mm, length 100 mm) under vacuum at room temperature, with 15 min acquisition time. Thin film surfaces were investigated using grazing incidence small-angle X-ray scattering (GISAXS) recorded under a shallow angle of 0.2°. Size distributions (without prior assumption of particle shape) were obtained from our scattering curves using the Monte Carlo based software package McSAS,[3] using a convergence criterion of 2, with 10 calculating repetitions and 500 contributions.

Photoluminescence: The photoluminescence (PL) spectra of the $FAPbBr_3$ NC films were measured using a Horiba Fluoromax-4 (slit width 0.4 nm and 0.1 s integration time), respectively. For the excitation spectra, the maximum PL emission peak was used (slit width 0.1-0.2 nm and 0.3-0.5 s integration time).

Absorbance: The absorbance spectra of the composite NC films were measured using a Shimadzu UV-2550 spectrophotometer with an integrating sphere attachment (20 nm slit width is used to collect transmitted photon).

Time-resolved photoluminescence (TR-PL): The micro-PL setup is based on fiber coupled microscope system, where the excitation path and the emission collection from the side, using a VIS-NIR microscope objective (10x, NA= 0.65). The samples were excited with 5-MHz-repetition-rate, picosecond-pulse light sources at 405 nm (Picoquant P-C-405B) light-emitting diode. The beam spot size was about 10 µm. Time-resolved decay curves were collected using an Acton monochromator (SpectraPro 2300), fiber coupled to the microscope, to filter the desired wavelength, and detected by Micro Photon Devices single-photon avalanche photodiode (LDH-P-670). The signal was then acquired by a time-correlated single photon counting card (Pico Harp TSCPC module and Picosecond Event Timer 300). The temporal resolution is ~50 ps. The decay curves were fitted with a double exponential function. The resulting decay components and the relative weights are reported in Table S10-S14.

Photoluminescence quantum yield (PLQY): PLQY dependencies on the excitation fluence were measured with a 2-inch integrating sphere (Thorlabs model IS200). Investigated samples were placed inside the sphere and excited using a semiconductor continuous-wave laser beam (200 mW full power) emitting at 405 and 447 nm. An optical fiber was attached to the sphere to direct the light to an Ocean Optics spectrometer. The excitation beam intensity was attenuated by means of calibrated neutral interference filters (Thorlabs).

Transient absorption: Visible pump visible probe transient absorption measurement was conducted using a Continuum IntegraC regenerative/multipass femtosecond amplifier system capable of generating <100 fs, 1 KHz and 2.5 mJ ultrashort pulse at 800 nm. Pump wavelength of 375 nm is generated by frequency doubled the 750 nm VIS2 output of a Continuum Pallitra OPA pumped with 1 mJ of the laser output. Two dielectric mirrors designed for 3rd harmonic of Nd:YAG laser are used as filter to remove fundamental 700 nm and any other residue output from the OPA. White light continuum is generated by focusing part of the amplifier output onto a constantly rotating CaF_2 with appropriate beam size and power control. To prevent oversaturation of the CCD spectrometer, a 700 nm shortwave pass filter is used to remove the excessive 800 nm generation beam. As a result, a stable smooth broadband white light continuum spanning 370-650 nm is generated. On the sample, the probe white light is focused via a parabolic mirror to a spot size of ~20 µm. A f = 250 mm UV fused silica (UVFS) lens is used to focus the pump beam onto the sample at its beam waist of ~100 µm diameter. To prevent sample degradation due to humidity and oxidation, the sample is taped onto a UVFS cuvette that has been filled with nitrogen. Longpass filters with cut-off wavelength of 375 nm were used to prevent scattered pump beam to enter the CCD spectrometer.

Global fitting: Global fitting is performed using the freely available Glotaran frontend[4] of the R-based TIMP global and target analysis software package.[5] The average of approx. -5 to -1 ps regime data are used for the baseline correction to remove the contribution of long lived fluorescence signal around the photobleaching peak and coherent artifacts were removed numerically using the built-in instrument response function (IRF) model. Dispersion of the white-light probe and IRF were removed by numerical fitting using the default ParMu model for dispersion and Gaussian IRF.

***Photoelectron spectroscopy in air (PESA)*:** Measurements on spin-coated NC thin films were conducted using a Riken Keiki AC-2 spectrometer with a power setting of 800 nW (power number of 0.5).

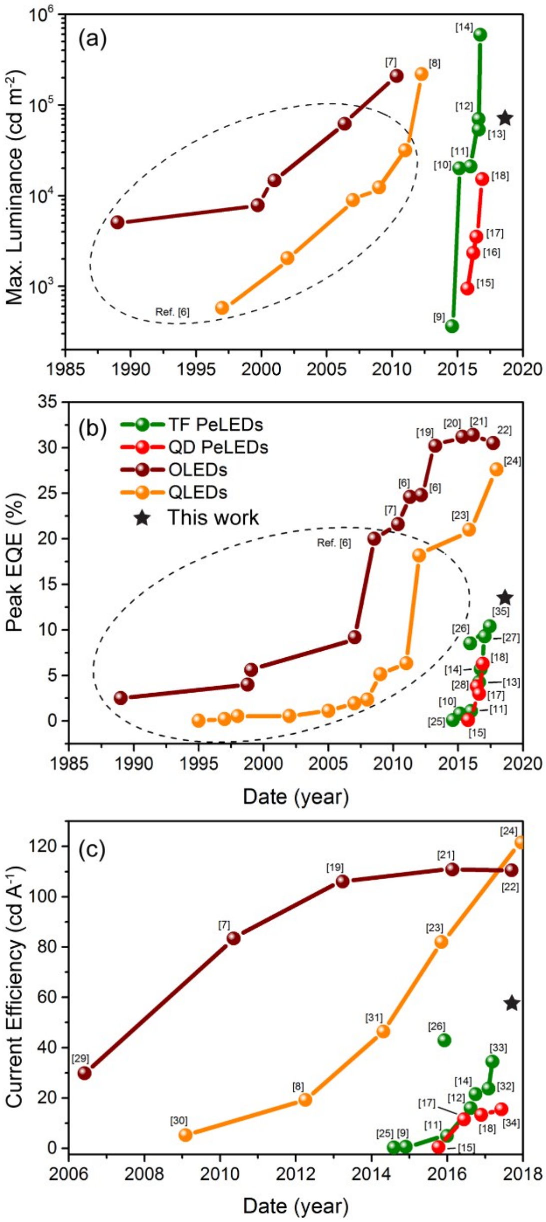

Fig. S1 Overview of best reported LED devices values for organic (OLED), semiconductor quantum dots (QLEDs), and perovskite (PeLED).[6-35] (a) Maximum luminance, (b) peak external quantum efficiency, and (c) current efficiency. Note: TF and QD refer to thin film and quantum dot (or nanoparticle) films. All perovskite device data is based on green-emitting materials. The star symbol represents the device performance demonstrated in this work. Most reported data points for QLEDs and OLEDs (within the dashed ovals) are derived from a recent review article by Shirasaki et al.[6] They represent the highest achieved device efficiencies and luminance (i.e. with or without out-coupling structures, inverted or normal structures). The data points in (a-c) for OLEDs are taken from references [6, 7, 19-22, 29]; data points in (a-c) for QLEDs are taken from references [6, 8, 23, 24, 30, 31]; data point for TF PeLEDs are taken from references [9-14, 25-27, 32, 33, 35]; and data point for QD PeLEDs are taken from references [15-18, 28, 34], respectively.

Fig. S2-S11: Device Fabrication, band alignment, stability, flexible/large area devices

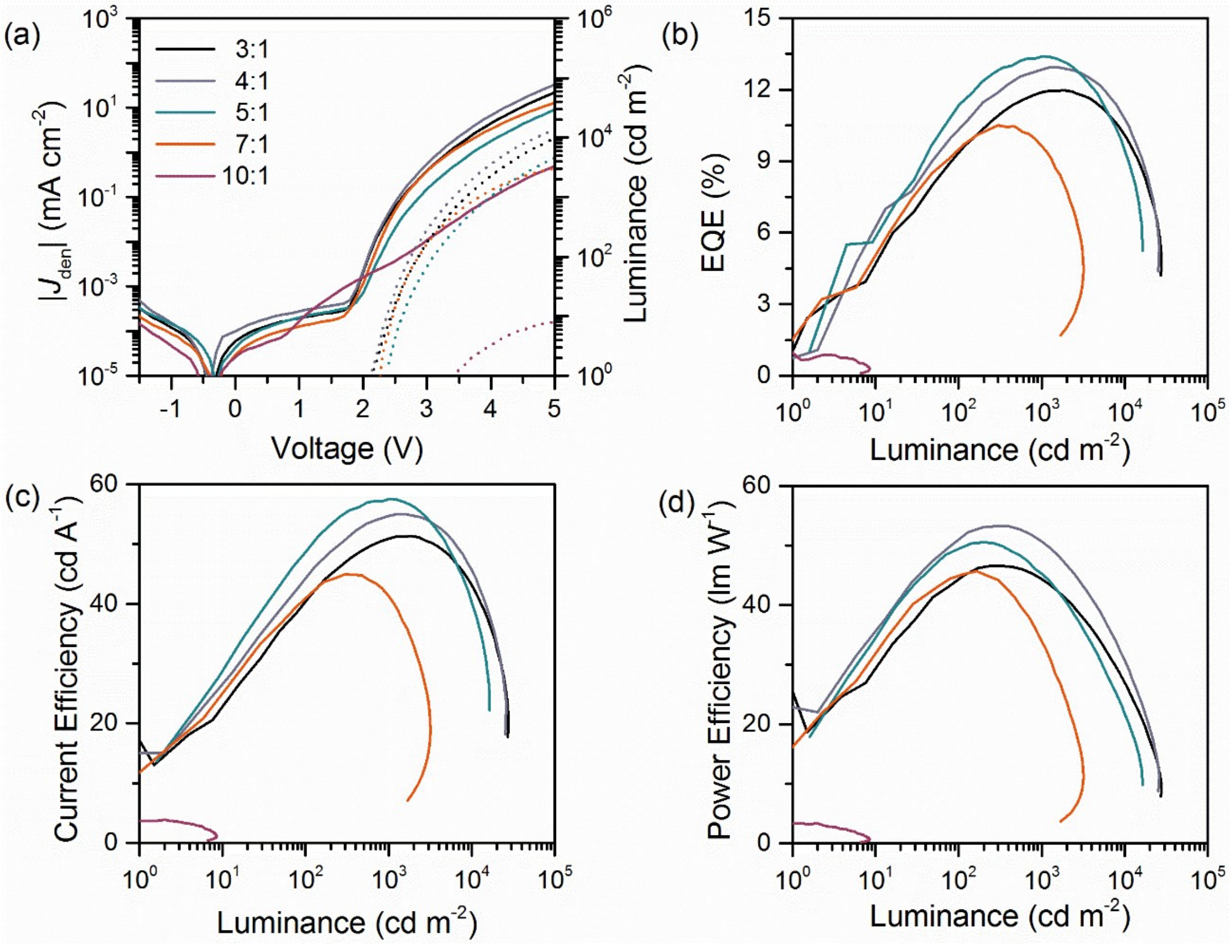

Fig. S2 LED device characteristics prepared with different OA:$PbBr_2$ ratios. (a) Current density-voltage-luminance characteristics, and (b) EQE, (c) current efficiency, and (d) luminous power efficiency versus luminance. The active device area is 3 mm^2. At low voltages (-1 V < V < 1 V), the measured current is smaller than 1 nA as a consequence of small device area (3 mm^2). The total current in this range are therefore inclusive of both charging and leakage currents from the coaxial cable, hence the slight shift of the zero current crossing towards negative voltages. The device parameters are summarized in Table 1 and S2.

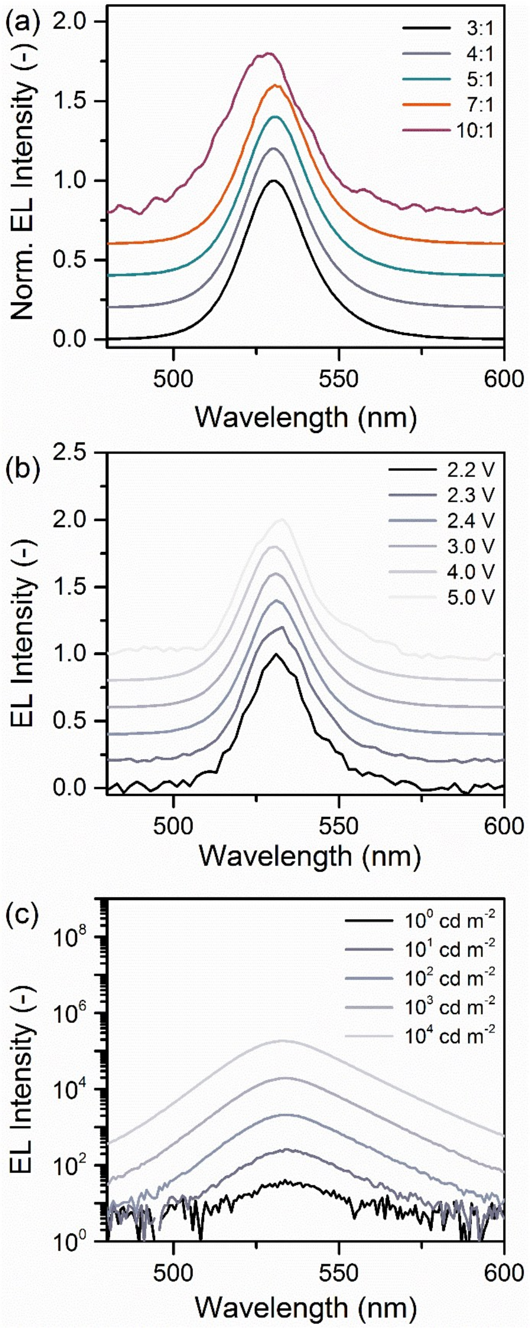

Fig. S3 Electroluminescence characteristics for (a) samples prepared with different OA:$PbBr_2$ ratios, (b) at different bias, and (c) at different luminance intensity. Devices in (b) and (c) are prepared with OA:$PbBr_2$ ratio 4:1. The active device area is 3 mm^2. (a) EL spectra collected at maximum luminance for different OA:$PbBr_2$ ratios are similar, except the slight blue-shift (3-5 nm) observed ratio 10:1. (b) Normalized EL spectra, collected at sub-energy-gap (2.2 V) and above energy gap bias (2.3-5 V), suggest that there is no sub-gap, trap-related EL emission at sub-energy-gap external voltage bias. (c) EL spectra at different luminance levels scale proportionally to the emission intensity, suggesting that the emissive species at different luminance are equal.

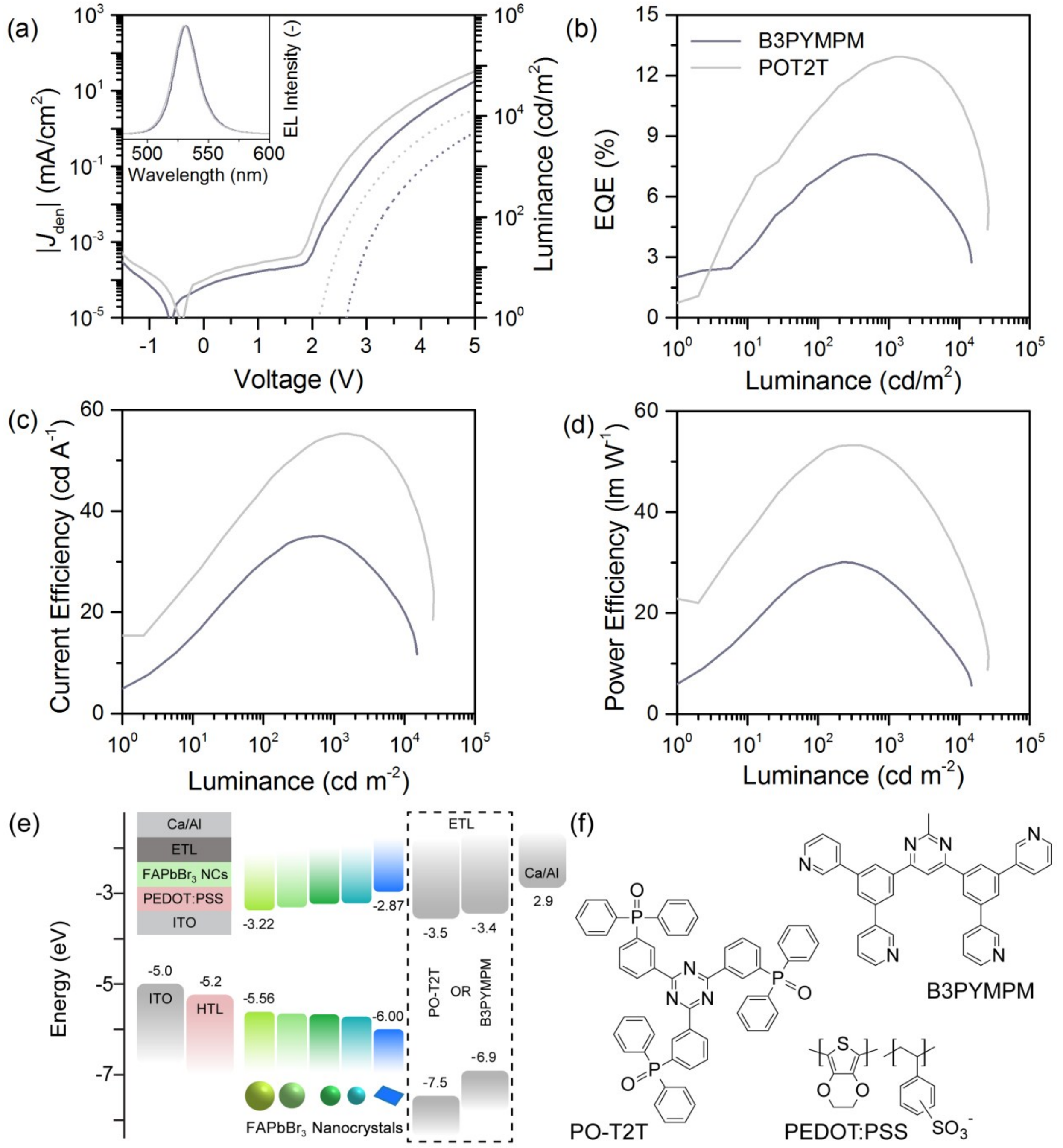

Fig. S4 LED characteristics with different electron transporting layers. (a) Current density-voltage-luminance characteristics of LED devices. The inset shows the electroluminescence spectra at maximum luminance. (b) Current efficiency, (c) EQE, and (d), luminous power efficiency as a function of luminance. (e) Band alignment of the device architecture and (f) the molecular structures of hole and electron transporting materials used in this work. The emissive layer is the perovskite nanocrystals synthesized with OA:PbBr$_2$ of 4:1. The device parameters are summarized in Table S4.

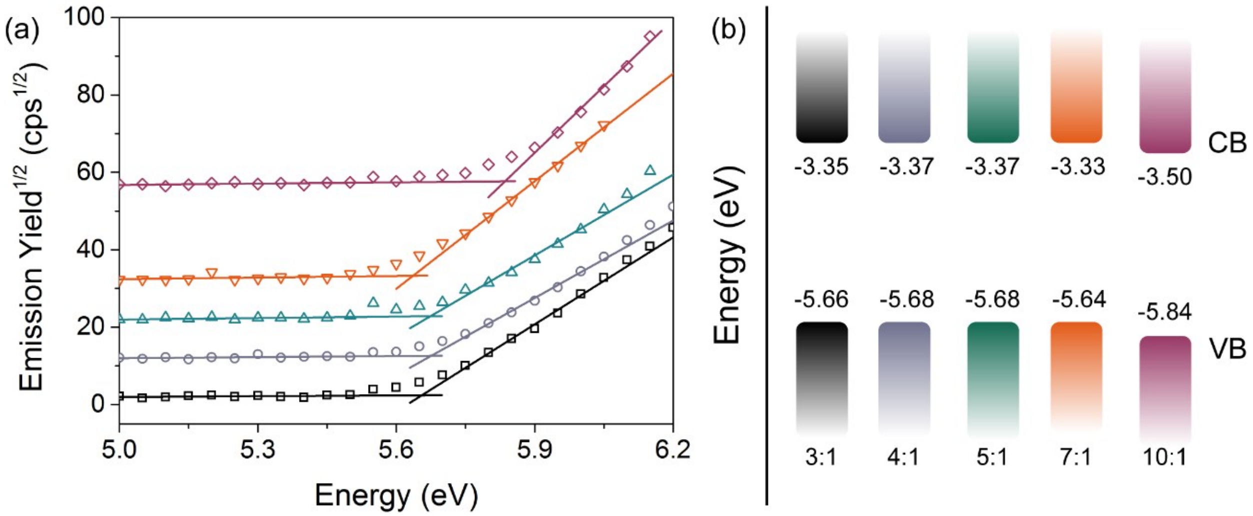

Fig. S5 Valence (VB) and conduction band (CB) level determination of $FAPbBr_3$ and $(OA)_2(FA)_{n-1}Pb_nBr_{3n+1}$ composite films using photoelectron spectroscopy in air. Here, the CB was calculated through addition of the optical bandgap and the VB. (a) PESA curves and respective fit curves, and (b) schematic representation of the band levels of samples prepared with different OA:$PbBr_2$ ratios.

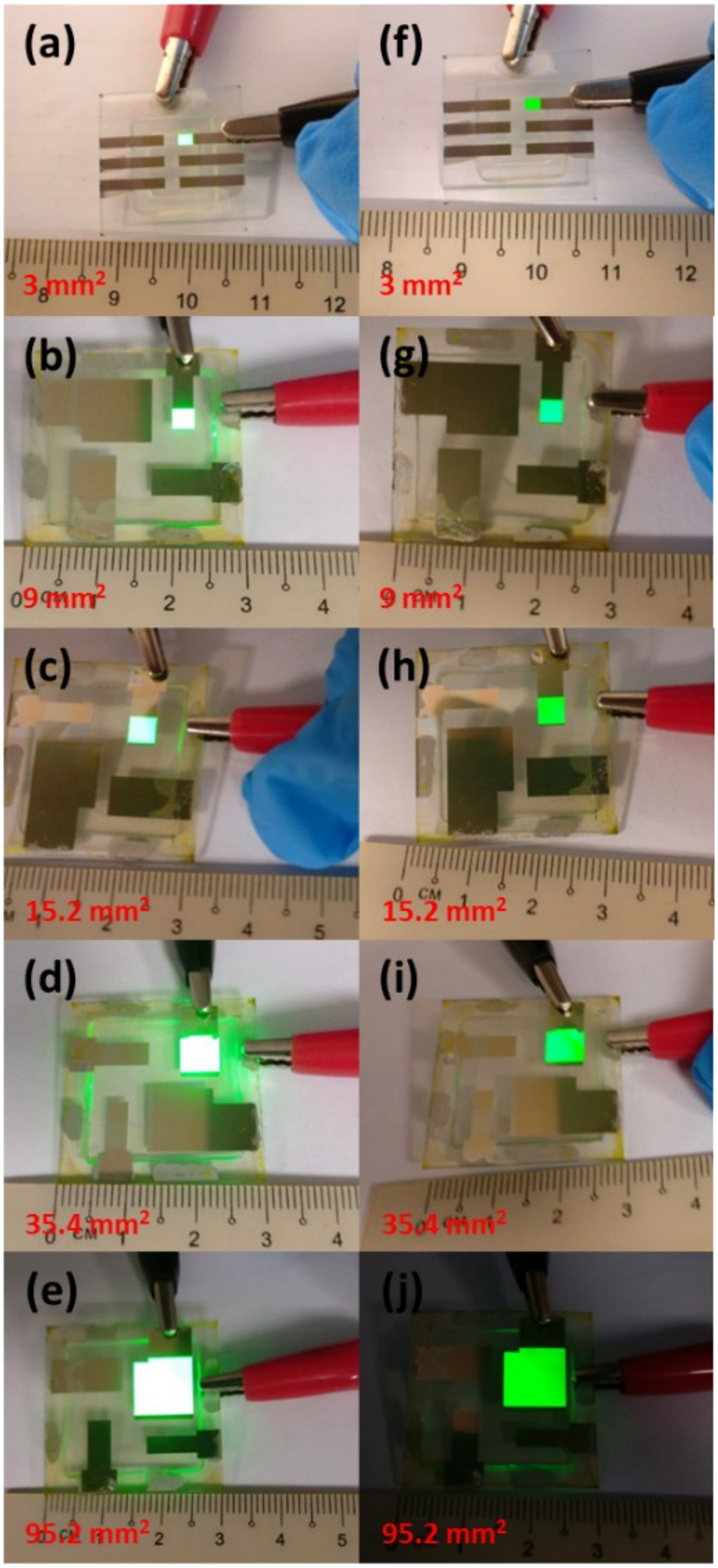

Fig. S6 Bright and uniform LED devices. (a-e) Bright luminescence of LED devices with different active area operating at 4.5 V. (f-j) Uniform emission from LED devices with different active area operating at 2.7 V.

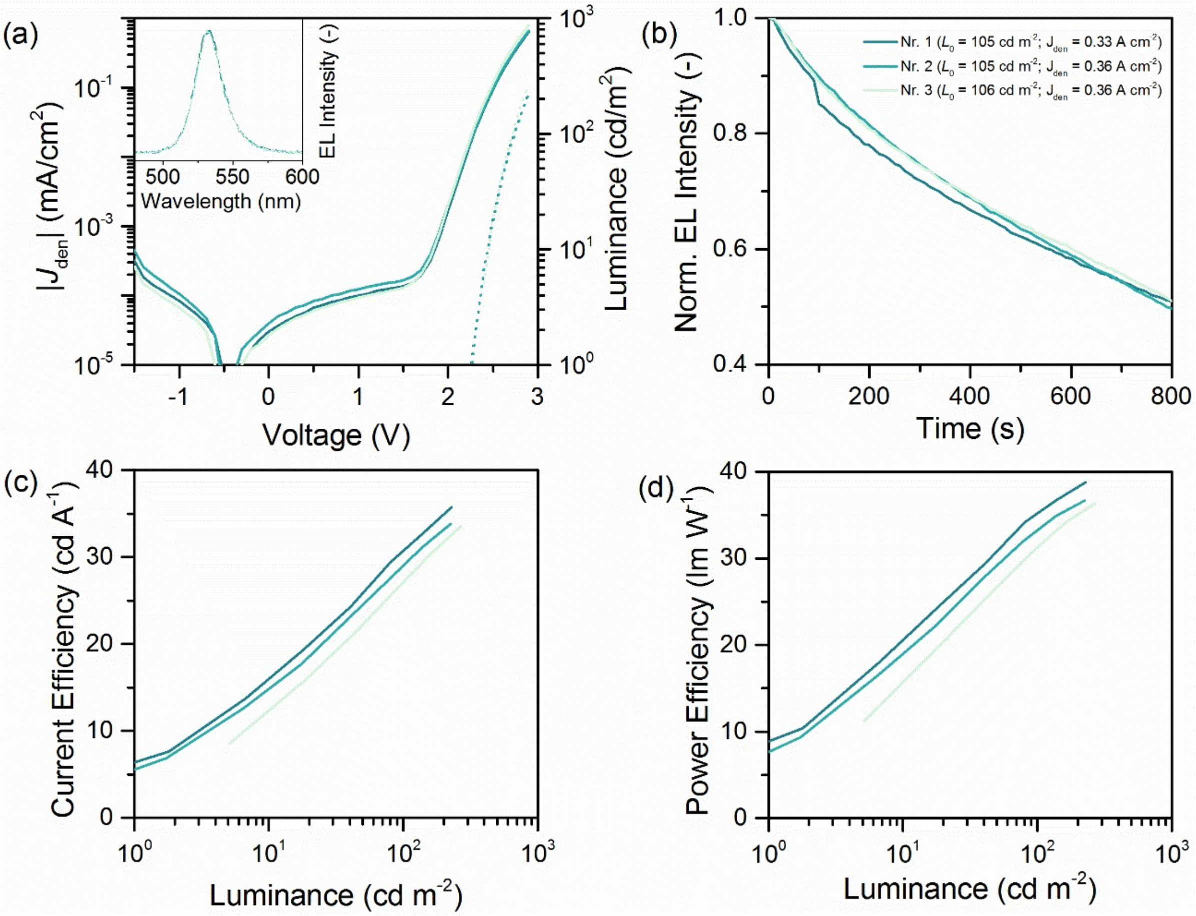

Fig. S7 LED device stability of three different devices under constant current bias. (a) Current-voltage-luminance characteristics. The inset shows the electroluminescence spectra at maximum luminance. (b) Constant current stability. The legend indicates the initial luminance L_0 and the current density applied to each device during the stability test. (c) Current efficiency and (d) luminous power density as a function of luminance of LED devices used for the constant current stability test. The device parameters are summarized in Table S3. The devices were measured by sweeping voltage biases up to 2.9 V before the constant current stability test. The emissive layer is the perovskite nanocrystals synthesized with OA:$PbBr_2$ of 5:1.

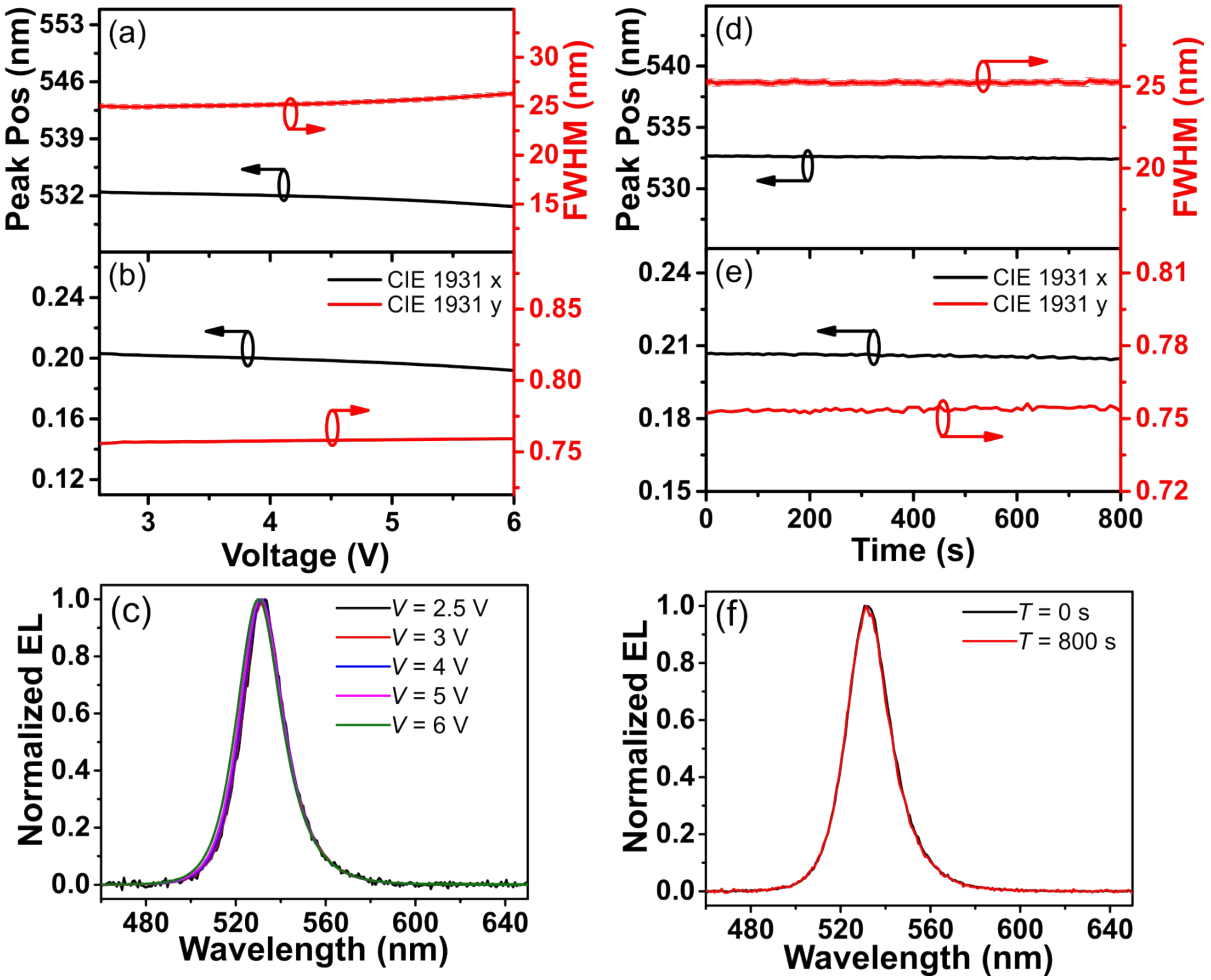

Fig. S8 Color stability of LED devices. (a) Peak position and FWHM, (b) CIE coordinate of electroluminescence spectra as a function of biased voltage. (c) Normalized electroluminescence spectra at selected bias voltages. (d) Peak position and FWHM, (e) CIE coordinate of electroluminescence spectra as a function of time of constant current measurement. (f) Normalized electroluminescence spectra at 0 s and 800 s of constant current measurement. The emissive layer is the perovskite nanocrystals synthesized with OA:$PbBr_2$ of 5:1.

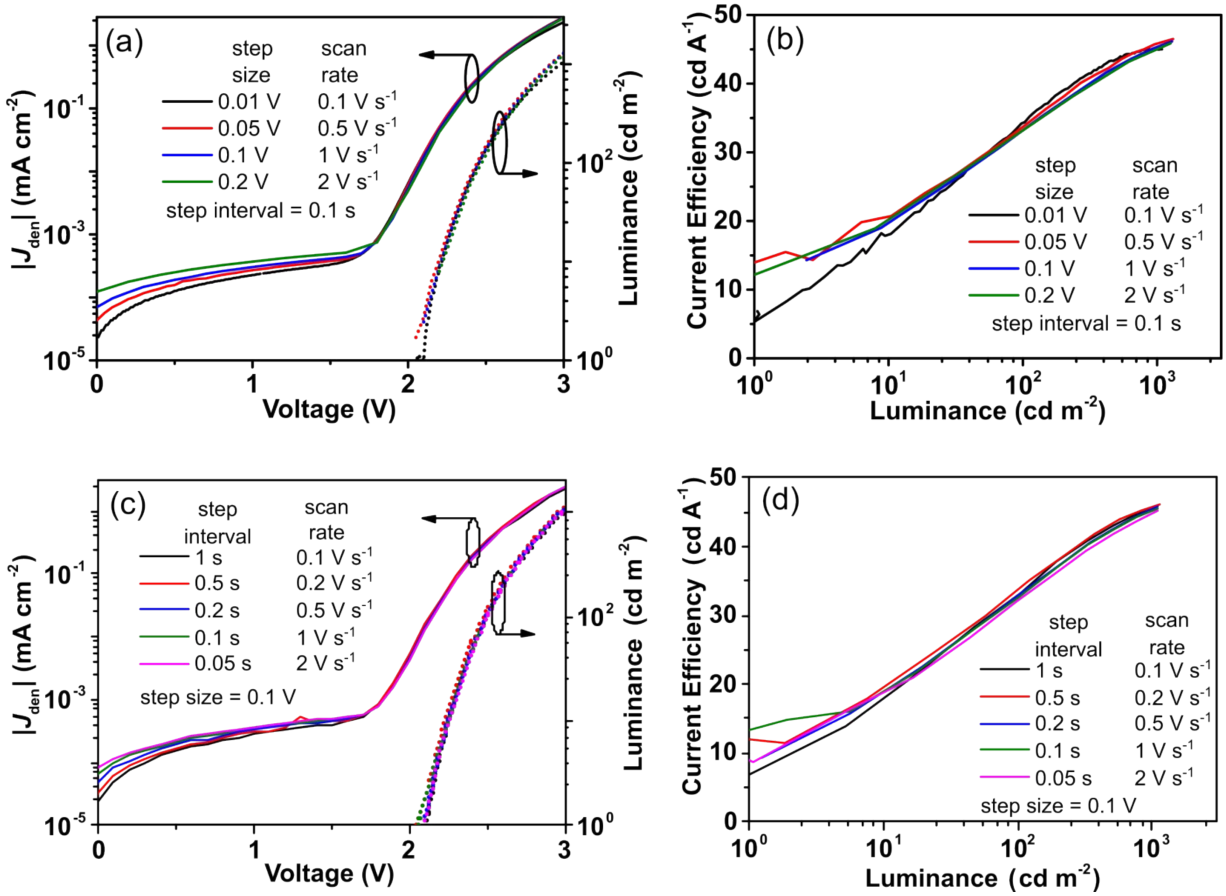

Fig. S9 LED characteristics as a function of scan rate. (a) Current-voltage-luminance characteristics and (b) current efficiency as a function of luminance of LED devices with different scan rate (fixed step interval, varying step size). (c) Current-voltage-luminance characteristics and (d) current efficiency as a function of luminance of LED devices with different scan rate (fixed step size, varying step interval). The emissive layer is the perovskite nanocrystals synthesized with OA:PbBr$_2$ of 5:1. The J-V-L and current efficiency vs luminance curves are nearly identical for all investigated scan rates. The collection duration required for lowest scan rate (0.1 V s^{-1}) are very well within the stability of the devices, which is shown to be around 14 minutes (Fig. S7(b)).

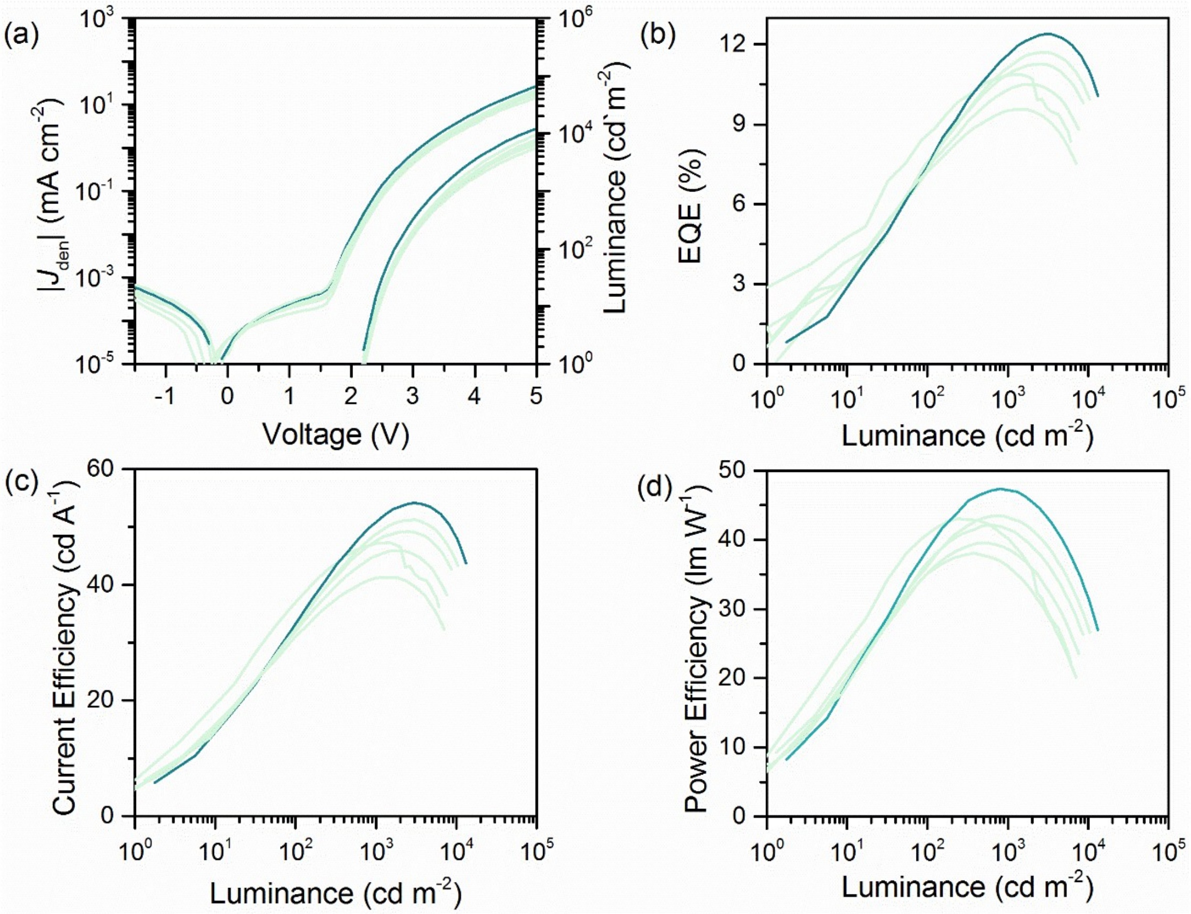

Fig. S10 Flexible LED device characteristics. (a) Current density-voltage-luminance characteristics, and (b) EQE, (c) current efficiency, and (d) luminous power efficiency versus luminance. The active device area is 3 mm^2. The emissive layer is the perovskite nanocrystals synthesized with OA:PbBr$_2$ of 4:1. The device parameters are summarized in Table S5 and S6.

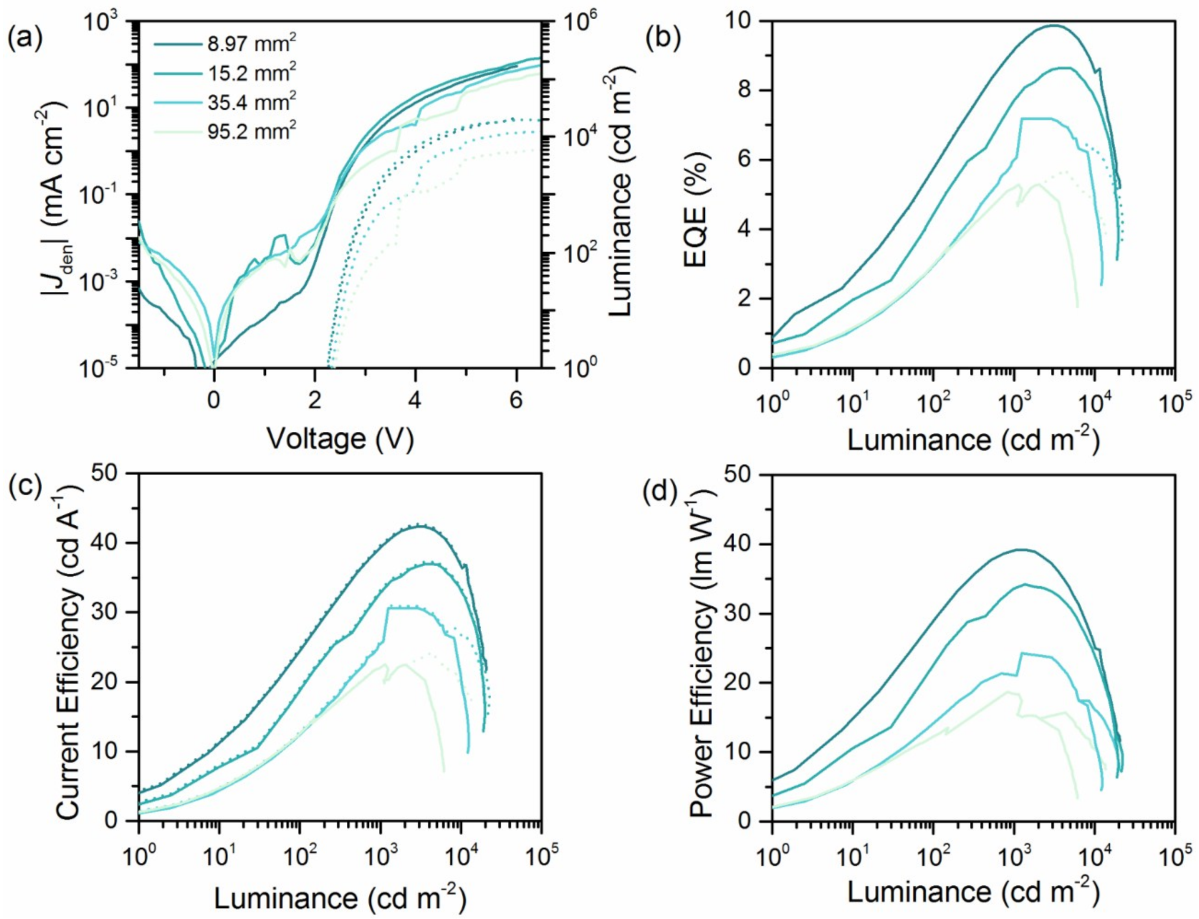

Fig. S11 Large area LED device characteristics. (a) Current density-voltage-luminance characteristics, and (b) EQE, (c) current efficiency, and (d) luminous power efficiency versus luminance. The solid lines represent the as-measured device characteristics, while the dotted lines represent the characteristics after correcting for the saturation of the spectrometer. The corrections are performed by scaling the luminance values linearly according to the spectral regions which did not saturate the spectrometer; under the assumption that the spectral shape remains unchanged at any given injection density. Note: the largest area device (95.2 mm^2) is larger than the opening of the integrating sphere (78.5 mm^2). The reported values are not corrected for the loss of photons (i.e. the photons not collected by the integrating sphere). The emissive layer is the perovskite nanocrystals synthesized with OA:$PbBr_2$ of 4:1. The device parameters are summarized in Table S7 and S8.

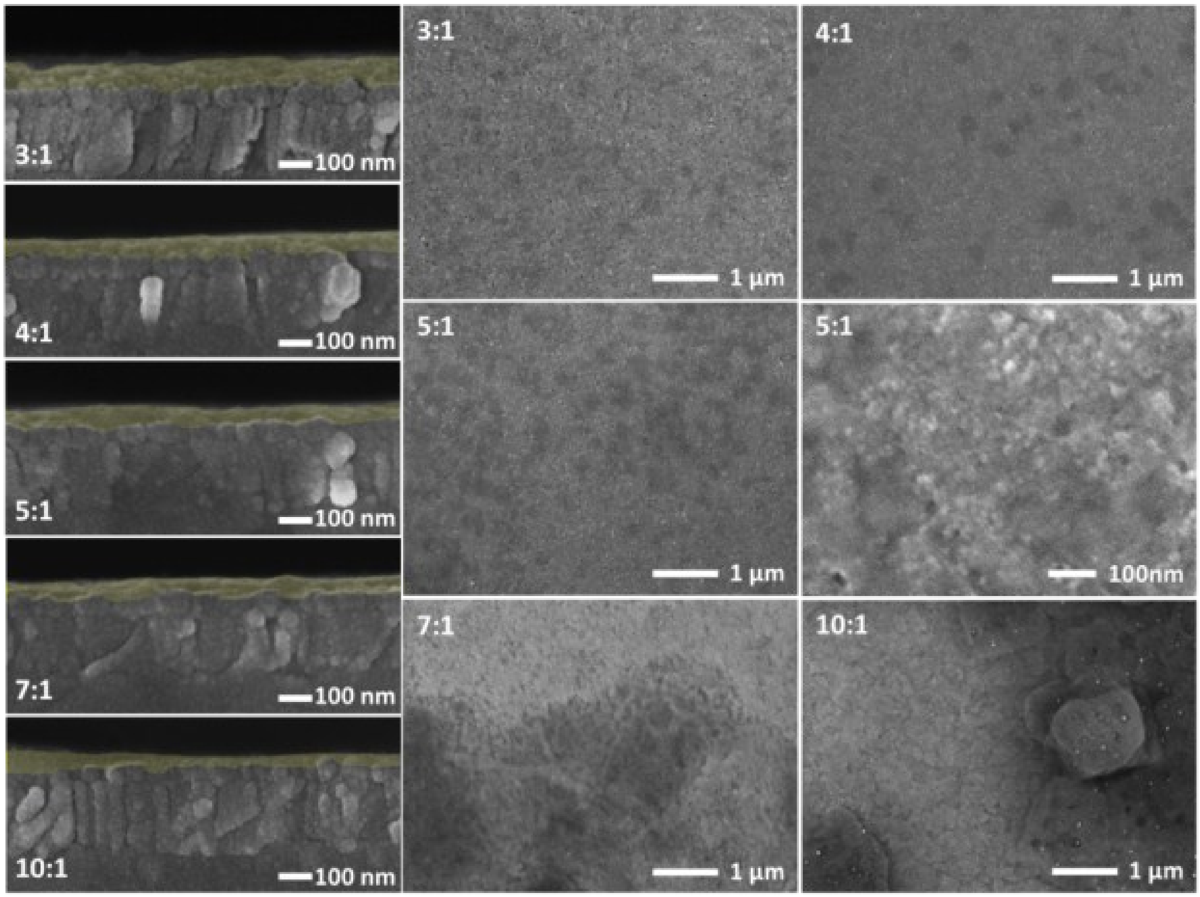

Fig. S12 Morphological investigation by FE-SEM of $FAPbBr_3$ and $(OA)_2(FA)_{n-1}Pb_nBr_{3n+1}$ composite films prepared with different OA:$PbBr_2$ ratios. Left panel: cross-sectional microscopy images of $FAPbBr_3$ nanoparticle films (colored). Right panels: top-view images showing an increased number of 2D MPLs (dark areas) for samples prepared with OA:$PbBr_2$ ratios up to 7:1. Increased ligand concentration resulted in the formation of mostly MPLs.

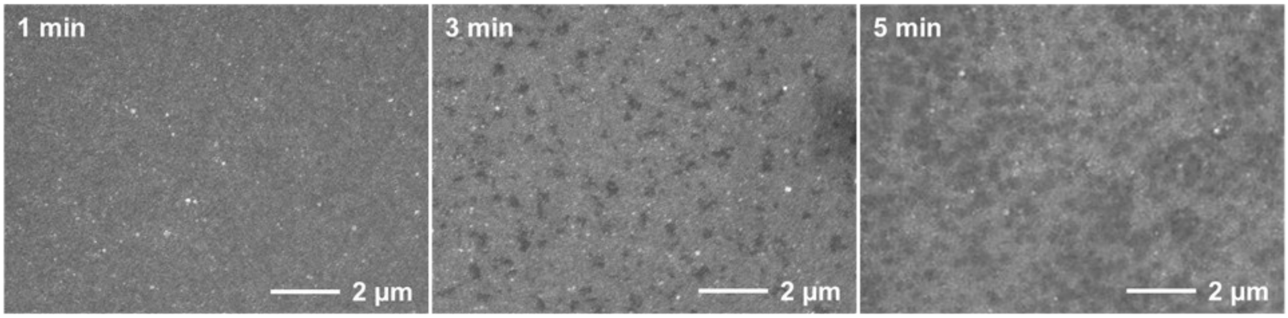

Fig. S13 SEM top surface images displaying the effect of longer waiting times between dropping the NC ink and the subsequent spin-coating. Longer waiting times results in a large concentration of MPLs (dark areas) on top of the NC thin film.

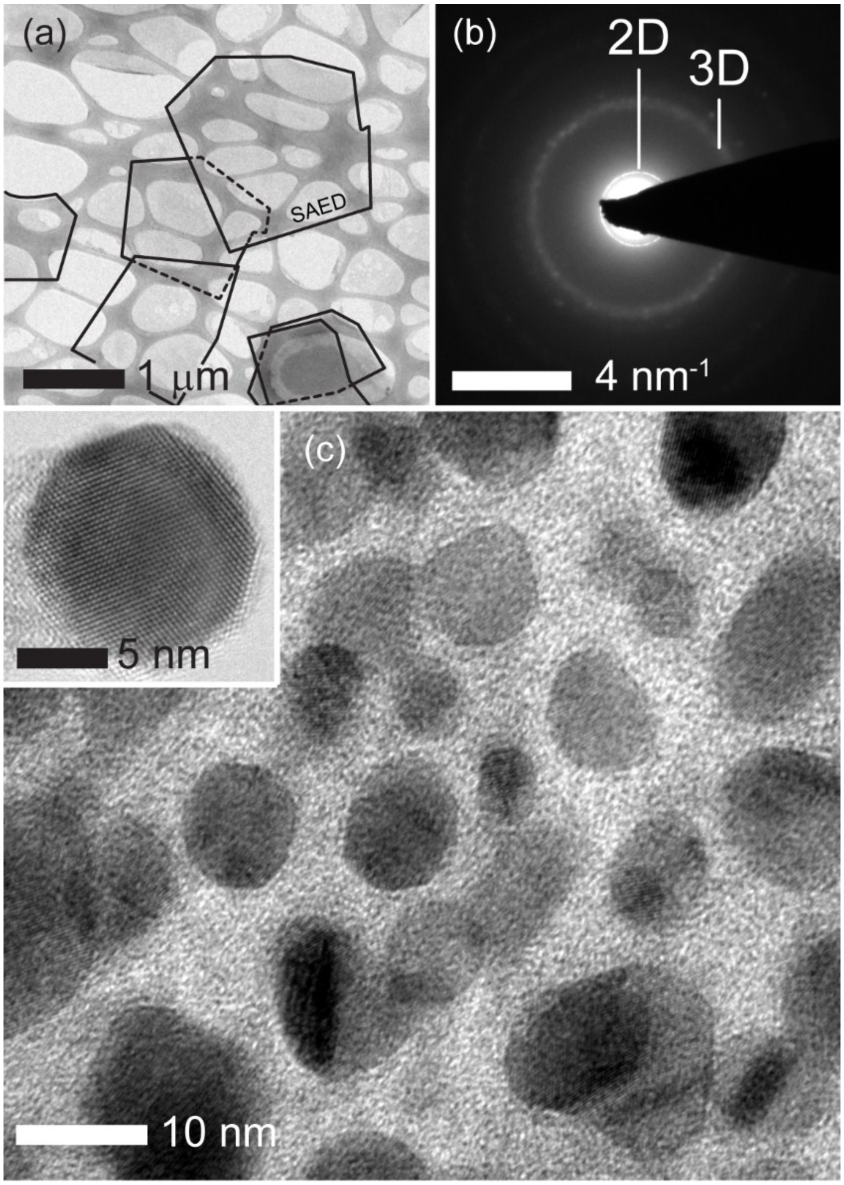

Fig. S14 STEM investigation of mixed-phase $FAPbBr_3$ and $(OA)_2(FA)_{n-1}Pb_nBr_{3n+1}$ NC inks dropcasted on a carbon-Cu grid with OA:$PbBr_2$ is 5:1. (a) The darker areas outlined with solid lines are $(OA)_2(FA)_{n-1}Pb_nBr_{3n+1}$ MPLs formed during the synthesis. (b) Selected-area electron diffraction pattern of marked area, exhibiting diffraction signals of both 2D and 3D phases. (c) Overview image of multiple NCs. The inset shows a crystalline $FAPbBr_3$ nanocrystal of approximately 10 nm diameter.

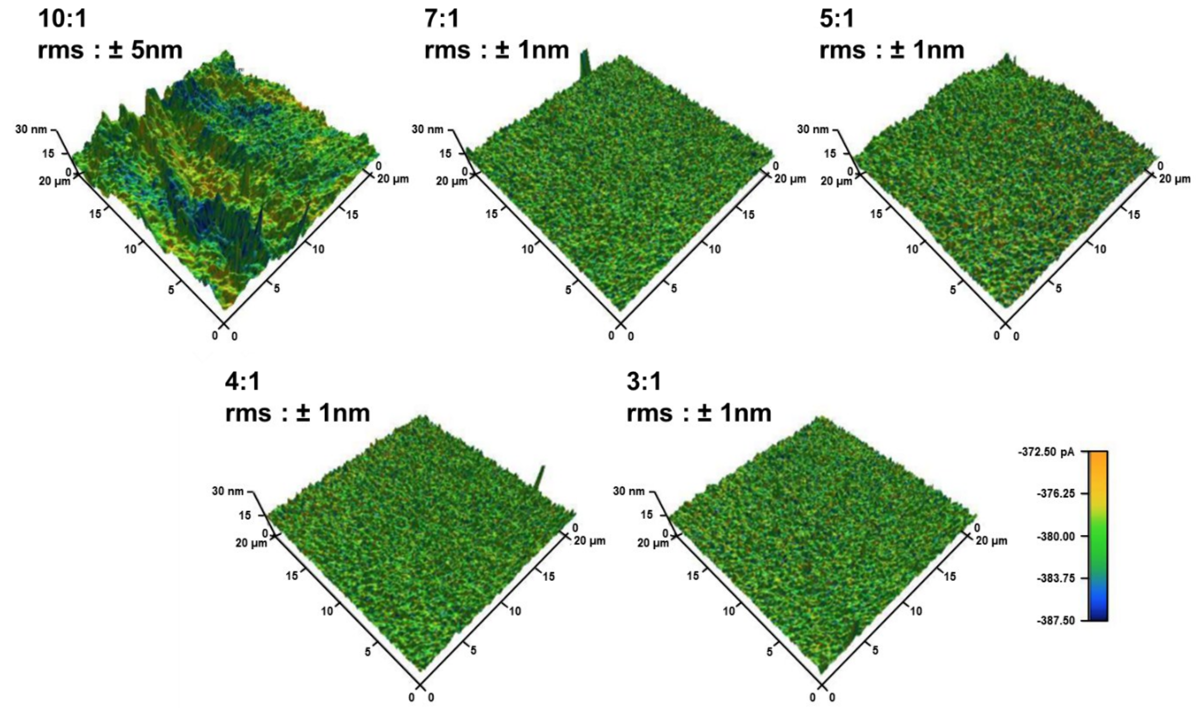

Fig. S15 Conducting AFM images of films synthesized using various amount of octylamine and $PbBr_2$ ratio. Current mapping was overlaid at the 3D surfaces of the film as color contour.

Fig. S16-S19: Optical and structural investigation of NC inks and composite thin films

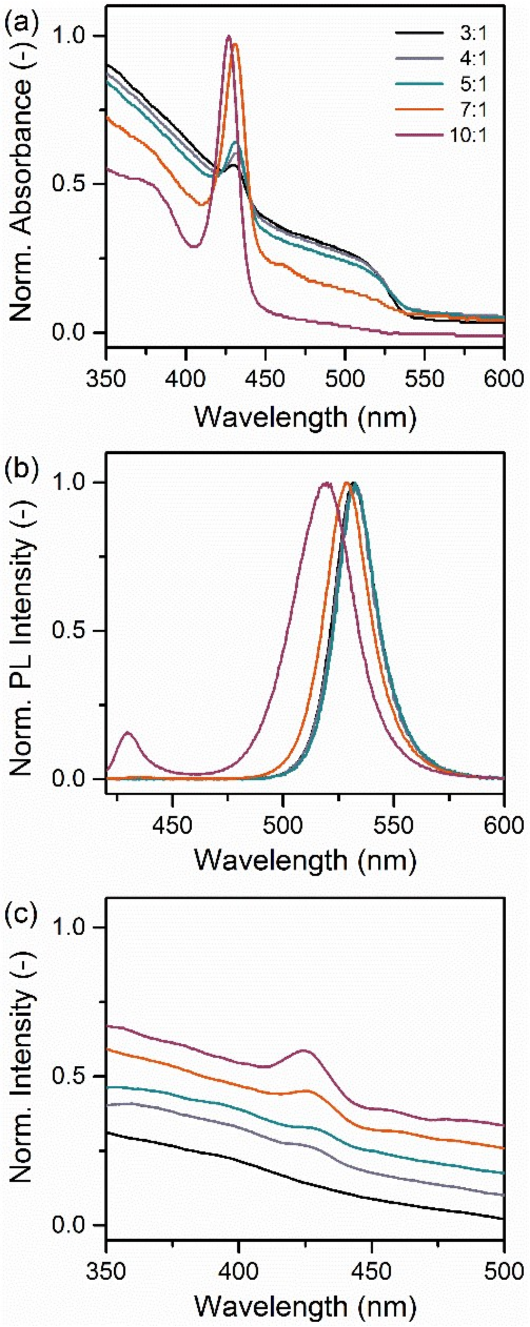

Fig. S16 Absorption, steady-state PL, and excitation spectra of thin film of mixed-phase NC inks synthesized with different OA:$PbBr_2$ ranging 3:1 (black) to 10:1 (purple).

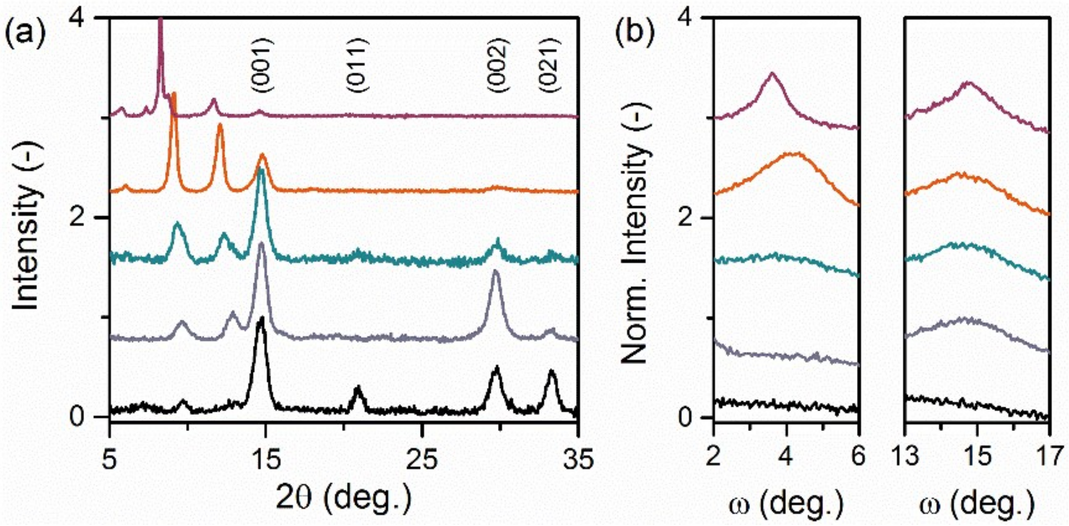

Fig. S17 (a) X-ray diffraction patterns and (b) rocking curves of self-assembled mixed-phase $FAPbBr_3$ and $(OA)_2(FA)_{n\text{-}1}Pb_nBr_{3n+1}$ thin films prepared with OA:$PbBr_2$ ranging 3:1 (black) to 10:1 (purple). Left panel: rocking curves of (001) reflection of $(OA)_2(FA)_{n\text{-}1}Pb_nBr_{3n+1}$ at 2θ ~9.6°. Right panel: rocking curves of (002) reflection of $FAPbBr_3$ at 2θ ~29.8°.

Small-angle X-ray scattering (SAXS). With SAXS, local electron density inhomogeneities are recorded at very small angles, which allows to extract structural information on length scales typically < 200 nm.[36] These density fluctuations may arise from a homogeneous suspension of nanocrystals (with electron density ρ) in a solvent matrix of different electron density, ρ_0 (or similarly from porosity within a particle). Conventionally, $I(q)$ is plotted versus the magnitude of the scattering vector, q, and is related to the scattering angle (2ϑ) and the wavelength (λ) of the incident beam via:

$$q = \frac{4\pi}{\lambda}\sin\theta \qquad \text{Equation 1}$$

In the case of dispersed NCs, the recorded scattering intensity $I(q)$ is proportional to the square of electron density difference, $(\Delta\rho)^2$, between the particles and the solvent matrix. Here, the scattered intensity may arise from the internal electron interference of individual nanocrystals (intraparticular), or from the electrons in an assembly of particles (interparticular), and can be written as a function of a form factor, P(q), and/or a structure factor, S(q), respectively. The total scattered intensity is then:

$$\mathrm{I}(q) = N \cdot (\Delta p)^2 \cdot P(q) \cdot S(q) \qquad \text{Equation 2}$$

where N is the number density of particles, and $(\Delta\rho)^2$ the scattering contrast. For dilute systems, the distance between individual particles is substantial and no interparticular interference is expected, *i.e.* $S(q) = 1$. The scattering intensity is then only proportional to the shape (form) of the particles. For smooth, solid spheres, P can be written as:

$$\mathrm{P}(q, r_0) = \left[3 \cdot \frac{\sin(q \cdot r_0) - q \cdot r_0 \cdot \cos(q \cdot r_0)}{(q \cdot r_0)^3} \right]^2$$

Equation 3

Here, r_0 is the radius of the smallest scattering particles. The contribution of these smallest scatterer is visible at high q values ($q \cdot r_0 >> 1$), when the slope decreases asymptotically according to $I(q) \propto q^{-4}$ (Porod's law).[37] At low q values, the scattered intensity is predominantly determined by the scattering of large particles or aggregates, and is described by the Guinier approximation:[38]

$$I(q) = I_0 \cdot \exp\left[-\frac{(q \cdot R_g)^2}{3} \right] \quad (\text{for } q \to 0)$$

Equation 4

The radius of gyration, R_g, is defined as the root-mean square center-of-mass distances within a particle or an assembly of particles. It can be determined from the slope in a plot of q^2 vs $\ln I(q)$; valid for $q \cdot R_g << 1$.

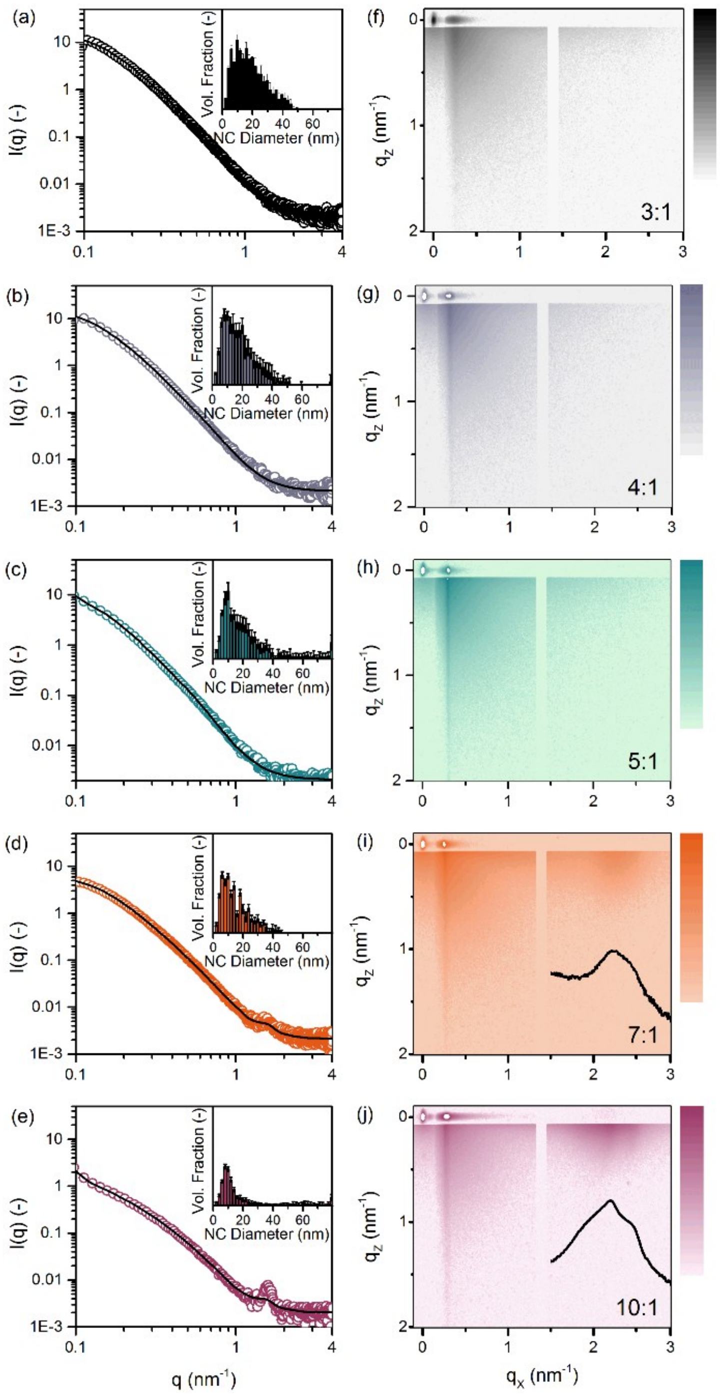

Fig. S18 Scattering curves of mixed $FAPbBr_3$ and $(OA)_2(FA)_{n-1}Pb_nBr_{3n+1}$ NC inks (a-e) and their self-assembled thin films (f-j) prepared with OA:$PbBr_2$ ranging 3:1 (black) and 10:1 (purple), respectively. (a-e) Small-angle x-ray scattering (SAXS) curves of NC inks, showing a Bragg reflection of 2D MPLs (at q ~1.60 nm^{-1} (equivalent to a d-spacing of approx. 3.93 nm) at OA:$PbBr_2$ ratios > 7:1. Insets: particle size distributions extracted from the scattering curves. (f-j) Grazing-incidence small-angle x-ray scattering (GISAXS) plots of the thin film top-surfaces, exhibiting perpendicular alignment of 2D $(OA)_2(FA)_{n-1}Pb_nBr_{3n+1}$ platelets (at q_X >1.5 nm^{-1}) with respect to the substrate's surface. The black curves in (i,j) represent the integrated peak area for $1.5 < q_X < 3$ nm^{-1}.

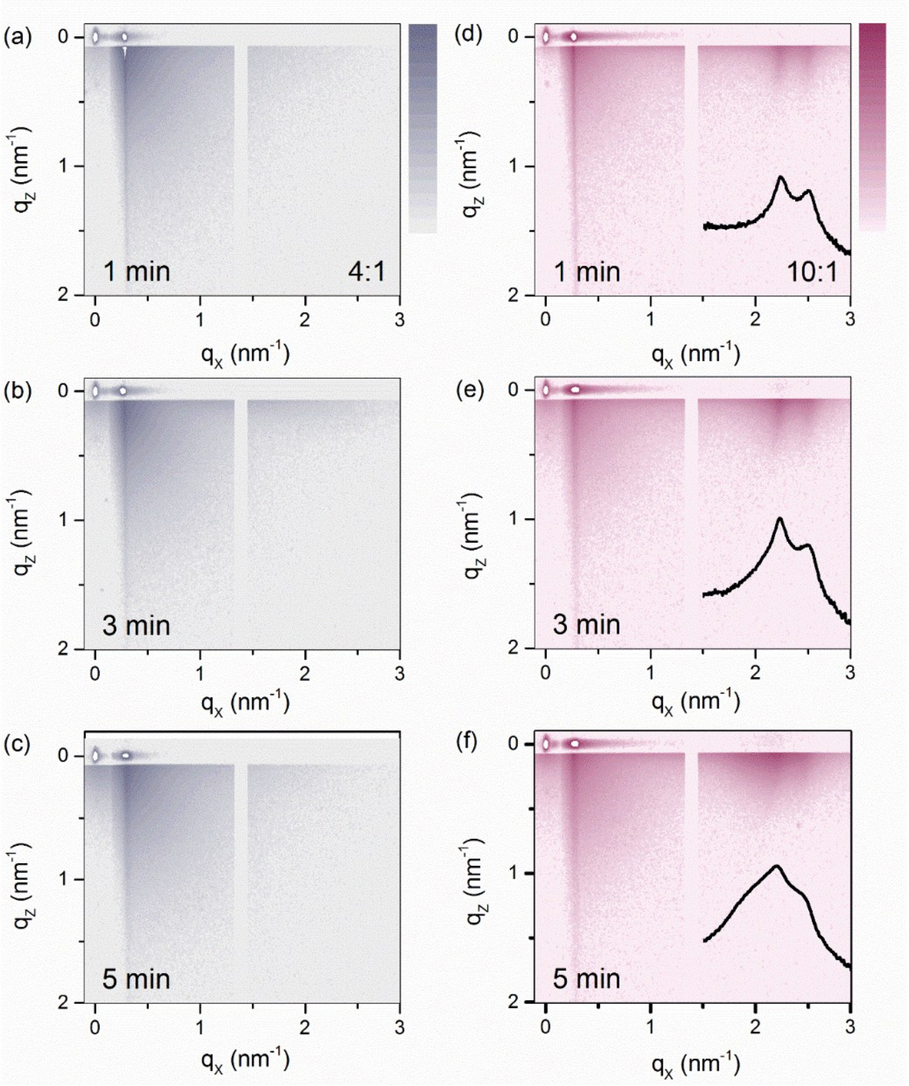

Fig. S19 Grazing-incidence small-angle x-ray scattering (GISAXS) plots of self-assembled mixed-phase $FAPbBr_3$ and $(OA)_2(FA)_{n-1}Pb_nBr_{3n+1}$ thin films prepared with OA:$PbBr_2$ 4:1 (a-c) and 10:1 (d-f), respectively. The NC inks were dropcasted on top of the ITO/PEDOT:PSS substrate layers and left for 1 to 5 min to initiate NC self-assembly, prior to spin-coating for 1 min at 1000 rpm. The 2D $(OA)_2(FA)_{n-1}Pb_nBr_{3n+1}$ platelets exhibit parallel alignment with respect to the substrate's surface, as observed by the peak formation at q_X >1.5 nm^{-1}. From the changes in the integrated peak shape and position, represented by the black curves in (d-f), it is evident that the $(OA)_2(FA)_{n-1}Pb_nBr_{3n+1}$ platelets self-assemble at longer waiting times.

Fig. S20-S21: Transient absorption characteristics

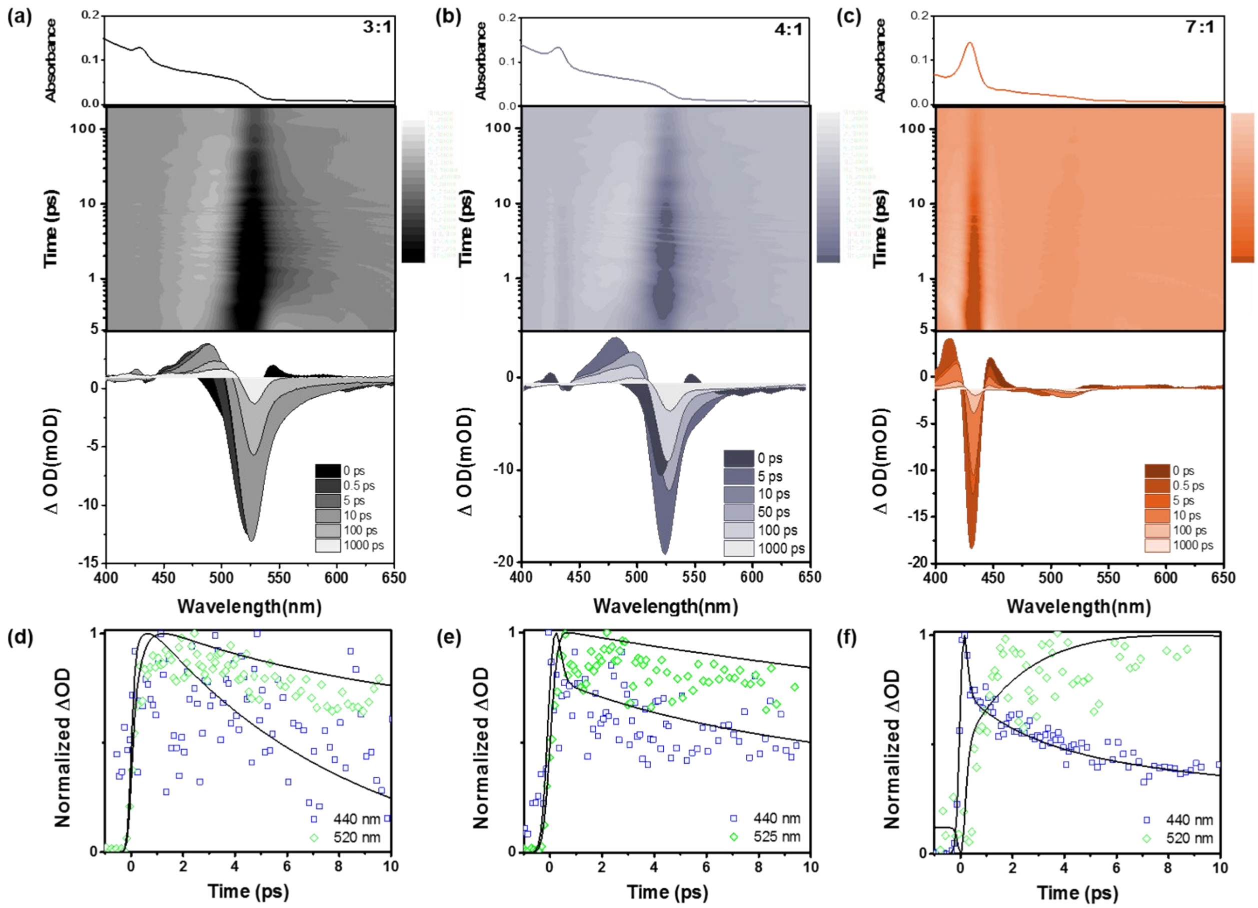

Fig. S20 Transient absorption (TA) spectra of FAPbBr$_3$ NCs. (a-c) UV-Visible absorption spectra (top) panel. TA mapping with excitation at λ=375 nm, 150 fs, and 1 μJ cm^{-2} fluency in the 0-200 ps range (central panel) and the relative TA spectra up to 1000 ps (lower panel) for FAPbBr$_3$ NCs prepared with 3:1 (a), 4:1 (b) and 7:1 (c) of OA: PbBr$_2$. Normalized kinetics of the TA signal at 440 nm and 520 nm for FAPbBr$_3$ NCs prepared with 3:1 (d), 4:1 (e), and 7:1 (d) of OA:PbBr$_2$.

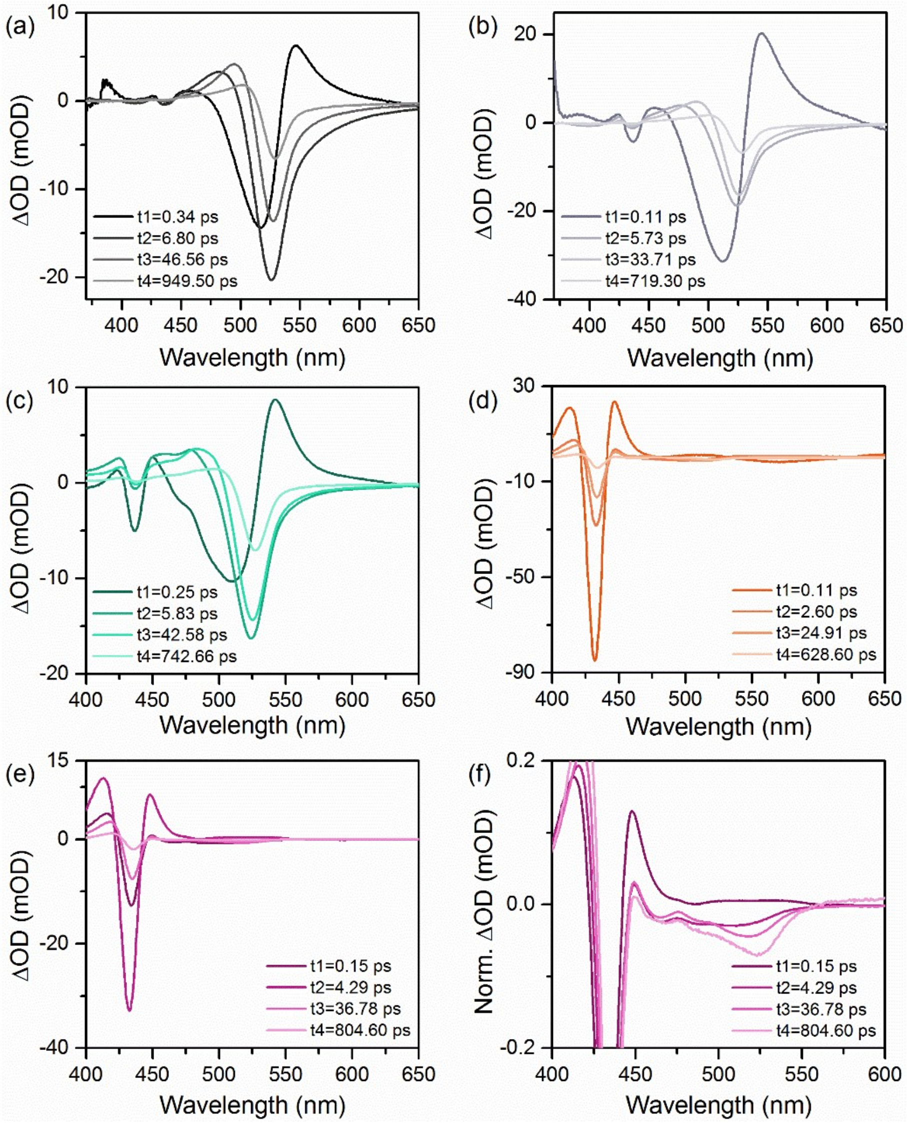

Fig. S21 TA spectra global fitting. (a-e) Spectral contribution at the characteristic decay times, obtained by the global fitting procedure for samples prepared with OA:$PbBr_2$ ratios of 3:1, 4:1, 5:1, 7:1, and 10:1, respectively. (f) is a zoom of (e) to highlight the photobleaching contribution at ca. 525 nm. A tabulated decay times for the global fitting result is also shown in Table S9.

Fig. S22-S24: Cathodoluminescence and time-resolved PL

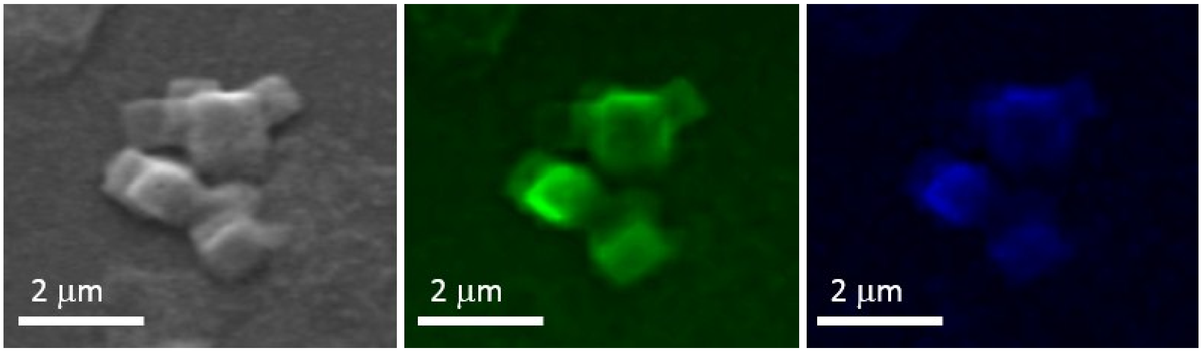

Fig. S22 Cathodoluminescence images of a spin-coated NC film (5:1 of OA: $PbBr_2$) on a silicon substrate. Images are taken using an electron beam of 5 keV energy, current of ~11nA, and exposure time of 10 ms. The CL images of middle and right panel are obtained by mapping with emission wavelength at 525 nm and 440 nm, respectively.

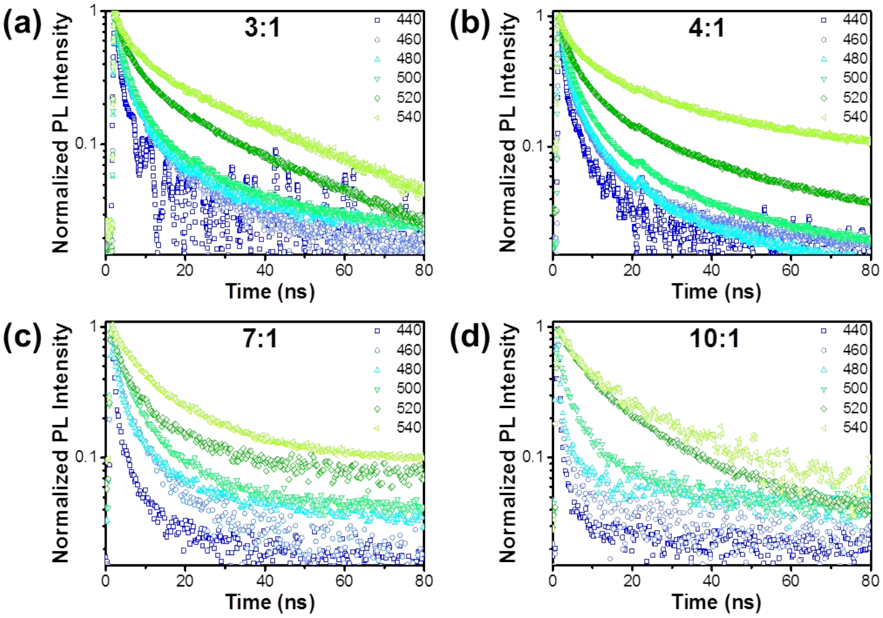

Fig. S23 Time-resolved photoluminescence dynamics of NC thin films with different OA:$PbBr_2$ ratios. (a-d) PL dynamics of NCs 3:1 (a), 4:1 (b), 7:1 (c), and 10:1 (d) with excitation wavelength 405 nm. The legend indicates the emission wavelength in nm. The resulting decay components and the relative weights are reported in Table S10-S14.

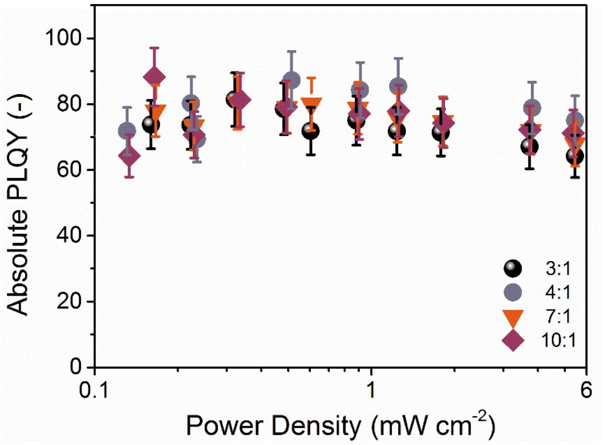

Fig. S24 Normalized photoluminescence quantum yield (PLQY) of nanocrystal thin film as a function of the excitation fluence for different OA:$PbBr_2$ ratios. The measurement error is approximately 5-10%.

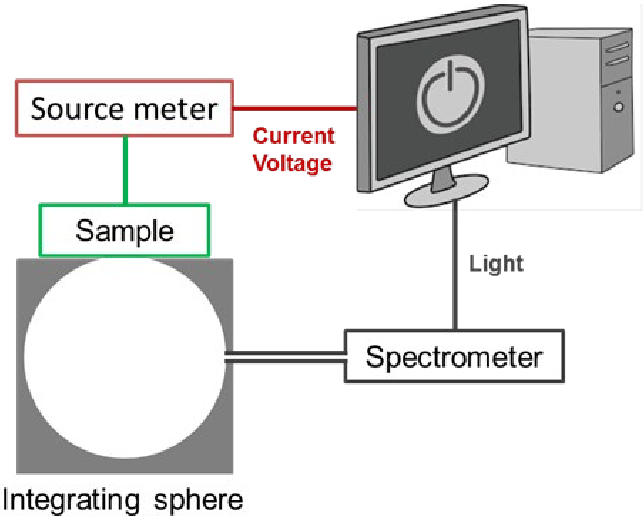

Fig. S25 Experimental setup for LEDs characterization. A Keithley 2612B was used to obtain the current-voltage characteristics of the LED devices. The emission from LEDs was collected by an integrating sphere (OceanOptics FOIS-1) coupled to a calibrated spectrophotometer (OceanOptics QEPro). An OceanOptics HL-3 Plus vis-NIR light source, calibrated using a procedure and documentation patterned after the ISO 17025, IEC Guide 115 and JCGM100:2008 (GUM) protocols, is used to calibrate the absolute irradiance measurement of the spectrometer. As LED devices are placed on the outside the integrating sphere, only forward emission is captured while the edge emission contribution is loss outside the integrating sphere.

Table S1 Overview of selected representative results of light-emission from organic-inorganic and all-inorganic halide perovskite in LEDs.

Perovskite Emitter[a]	Morphology	Device Architecture[b][c]	EQE	CE	L_{max}	V_T	Publication Date
			[%]	[cd A^{-1}]	[cd m^{-2}]	[V]	[-]
$CH_3NH_3PbBr_3$[25]	Thin film	ITO/PEDOT:PSS/Pe/F8/Ca/Ag	0.1	0.3	364	3.3	2014-08
$CH_3NH_3PbBr_3$[9]	Thin film	ITO/Buf-HIL/Pe/TPBI/LiF/Al	0.125	0.57	417	~4	2014-11
$CH_3NH_3PbBr_3$[39]	Thin film	ITO/PEDOT:PSS/Pe/ZnO/Ca/Ag	n.r.[d]	~21	~550	2	2015-01
$CH_3NH_3PbBr_3$[40]	Thin film	ITO/PEDOT:PSS/Pe-PIP/F8/Ca/Ag	1.2	n.r.	~200	n.r.	2015-02
$CH_3NH_3PbBr_3$[10]	Thin film	ITO/ZnO-PEI/Pe/TFB/MoO_x/Au	0.8	n.r.	~20,000	2.8	2015-04
$CH_3NH_3PbBr_3$[41]	Thin film	ITO/PEDOT:PSS/Pe/SPB-02T/LiF/Ag	0.1	0.43	3,490	~2.4	2015-11
$CH_3NH_3PbBr_3$[42]	NPLs	ITO/PEDOT:PSS/Pe/PVK:PBD/BCP/LiF/Al	0.48	n.r.	10,590	3.8	2015-11
$CH_3NH_3PbBr_3$[26]	Thin film	Glass/SOCP/Pe/TPBI/LiF-Al	8.53	**42.9**	~15,000	~4	2015-12
$CH_3NH_3PbBr_3$[11]	Thin film (printed)	ITO/Pe-PEO/Ag NWs	1.1	4.91	21,014	2.6	2015-12
$CH_3NH_3PbBr_3$[17]	Nanoparticle	ITO/PEDOT:PSS/Pe/TPBI/Cs_2CO_3/Al	3.8	11.5	11,830	2.8	2016-06
$CsPbBr_3$[13]	Thin Film	ITO/PEDOT:PSS/Pe-PEO/TPBI/LiF/Al	4.26	15.67	53,525	2.6	2016-08
$CsPbBr_3$[28]	Nanoparticle	ITO/PEDOT:PSS/PVK/Pe/TPBI/LiF/Al	3	8	330	3	2016-08
$CH_3NH_3PbBr_3$[12]	Thin film	ITO/NiO_x/Pe/TPBi/LiF/Al	n.r.	15.9	~70,000	~3.5	2016-08
$CsPbBr_3$[14]	Thin film	ITO/Pe-polymer/In-Ga	5.7	21.5	**591,197**	2.2	2016-09
$CsPbBr_3$[18]	Nanoparticle	ITO/PEDOT:PSS/PolyTPD/Pe/TPBI/LiF/Al	6.27	13.3	15185	3.4	2016-11
$CH(NH_2)_2PbBr_3$[43]	Thin film	ITO/ZnO/Pe/PolyTPD/MoO_3/Al	1.16	2.65	13,062	**1.9**	2016-11
$CH(NH_2)_2PbBr_3$[44]	Nanoparticle	ITO/PEDOT:PSS/Pe/TPBI/Cs_2CO_3/Al	n.r.	6.4	2,714	2.8	2016-11
$CH_3NH_3PbBr_3(C_4H_{10}BrNH_2)$[27]	Thin film	ITO/PVK/Pe/TPBI/LiF/Al	9.3	17.1	~8000	~3.5	2017-01
$Cs_{10}(MA_{0.17}FA_{0.83})_{90}PbBr_3$[32]	Thin film	ITO/ZnO/Pe/NPD/MoO_3/Al	7.3	23.7	19,420	2.4	2017-02
$CH_3NH_3PbBr_3$[33]	Thin film	ITO/PEDOT:PSS/Pe/TPBI/LiF/Al	8.21	34.46	6950	~3.5	2017-03
$CsPbBr_3$[45]	Thin film	ITO/PEDOT:PSS/Pe/TPBI/LiF/Al	4.76	21.38	51,890	2.6	2017-05
$CH(NH_2)_2PbBr_3$[46]	Nanoparticle	ITO/Buf-HIL/Pe/TPBI/LiF/Al	2.05	9.16	~700	~3	2017-05
$CH_3NH_3PbBr_3$[34]	Nanoparticle	ITO/Buf-HIL/Pe/TPBI/LiF/Al	5.09	15.5	~1000	~3	2017-06
$Cs_{0.87}MA_{0.13}PbBr_3$[35]	Thin film	ZnO/PVP/Pe/CBP/MoO_3/Al	**10.4**	33.9	91,000	2.9	2017-06
$CH(NH_2)_2PbBr_3$[47]	Nanoparticle	ITO/PEDOT:PSS/PolyTPD/Pe-PMMA/3TPYMB/LiF/Al	3.04	13.02	2939	2.75	2017-08
$CH(NH_2)_2PbBr_3$ (this work)	**Nanoparticle**	**ITO/PEDOT:PSS/Pe/PO-T2T/Ca/Al**	**13.4**	**57.6**	**>56,000**	**2.2**	**2017-11**

[a] All perovskites display green emission unless stated differently.

[b] Pe = perovskite.

[c] **ITO** = In-doped SnO_2; **PEDOT:PSS** = poly(3,4-ethylenedioxythiophene):polystyrene sulfonate; **F8** = poly(9,9-dioctylfluorene); **Buff-HIL** = buffered hole-injection layer; **TPBI** = 2,2′,2″-(1,3,5-benzinetriyl)-tris(1-phenyl-1-H-benzimidazole); **TPD** = *N*,*N*′-bis(3-methylphenyl)-*N*,*N*′-diphenylbenzidine); **PIP** = poly(imide) polymer; **PEI** = poly(ethylenimine), **TFB** = poly(9,9-dioctyl-fluorene-co-*N*-(4-butylphenyl)diphenylamine); **EA** = ethanolamine; **SPB-02T** = blue copolymer, Merck Co.; **BCP** = bathocuproine; **PEO** = poly(ethyleneoxide); **PVK** = poly(9-vinylcarbazole); **PVK:PBD** = (poly(9-vinylcarbazole):2-(4-biphenylyl)-5-phenyl-1,3,4-oxadiazole), **PolyTPD** = poly[N,N′-bis(4-butylphenyl)-N,N′-bisphenylbenzidine]; **CBP** = 4,40-Bis(N-carbazolyl)-1,10-biphenyl; **3TPYMB** = Tris[2,4,6-trimethyl-3-(pyridin-3-yl)phenyl]borane; and **PO-T2T** = 2,4,6-Tris[3-(diphenylphosphinyl)phenyl]-1,3,5-triazine

[d] Not reported.

Table S2 Device performance at various luminances. The table summarizes the voltage applied, EQE, current efficiency, and luminous power efficiency at 100 and 1000 cd m^{-2} as shown in Fig. 1 and S2. The maximum values are listed, while the bracketed values show the average and standard deviation values. Data is not available for 10: 1 NC device since the maximum luminance does not reach 100 cd m^{-2}.

OA:PbBr$_2$ Ratio	No. of Devices	Voltage [V]		EQE [%]		Current Efficiency [cd A^{-1}]		Luminous Power Efficiency [lm W^{-1}]	
		@ 100 cd m^{-2}	@ 1000 cd m^{-2}	@ 100 cd m^{-2}	@ 1000 cd m^{-2}	@ 100 cd m^{-2}	@ 1000 cd m^{-2}	@ 100 cd m^{-2}	@ 1000 cd m^{-2}
3:1	20	3.0 (2.9±0.1)	3.7 (3.5±0.1)	9.9 (5.1±2.8)	11.9 (7.4±2.9)	42.3 (21.8±12.5)	51.2 (31.0±12.9)	45.8 (23.7±13.5)	44.2 (27.4±10.9)
4:1	49	2.9 (2.7±0.2)	3.6 (3.3±0.3)	10.9 (9.4±0.9)	12.9 (12.1±0.4)	47.0 (40.2±4.0)	55.3 (51.7±1.9)	52.8 (46.8±4.0)	58.1 (49.5±4.3)
5:1	34	3.6 (3.0±0.3)	4.8 (3.9±0.4)	11.6 (9.7±1.2)	13.4 (11.9±0.6)	49.9 (42.0±5.0)	57.6 (51.6±2.5)	51.0 (43.5±4.7)	48.4 (42.5±4.1)
7:1	23	3.7 (3.2±0.3)	5.5 (4.4±0.5)	9.7 (9.2±0.3)	9.4 (7.8±1.2)	41.7 (39.6±1.5)	40.2 (33.1±5.2)	45.2 (39.2±3.4)	32.4 (24.5±6.2)
10:1	14	N.A.	N.A.	N.A.	N.A.	N.A.	N.A.	N.A.	N.A.

Table S3. Summary of the device parameters of LED devices used for constant current test as shown in Fig. S7. The devices were measured by sweeping voltage biases up to 2.9 V before the constant current stability test.

Device Nr.	Maximum Luminance [cd m^{-2}]	Maximum Current Efficiency [cd A^{-1}]	Maximum Luminous Power Efficiency [lm W^{-1}]	Maximum EQE [%]
1	227	35.8	38.8	8.3
2	223	33.8	36.6	7.8
3	268	33.5	36.3	7.5

Table S4. Table summarizes the LED device characteristics with different electron transporting layers as shown in Fig. S4. The emissive layer consists of perovskite NCs synthesized with OA:PbBr$_2$ is 4:1.

Electron Transporting Layer	Turn-on Voltage [V]	Maximum Luminance [cd m^{-2}]	Maximum Current Efficiency [cd A^{-1}]	Maximum Luminous Power Efficiency [lm W^{-1}]	Maximum EQE [%]
B3PYMPM	2.7	14957	35.1	30.1	8.1
PO-T2T	2.2	25901	55.3	53.2	12.9

Table S5. Device characteristic parameters of flexible devices. Table summarizes the maximum luminance, current efficiency, luminous power efficiency, and EQE of flexible LED devices as shown in Fig. S10. The emission area is 3mm^2. The emissive layer is the perovskite nanocrystals synthesized with OA:PbBr$_2$ of 4:1.

N_{th} Device	Luminance [cd m^{-2}]	Current Efficiency [cd A^{-1}]	Luminous Power Efficiency [lm W^{-1}]	EQE [%]
1	7637	46.0	39.5	10.5
2	7030	41.6	38.0	9.6
3	6040	47.3	43.1	10.9
4	8611	49.2	42.1	11.3
5	13153	54.1	47.4	12.4
6	10475	51.2	43.5	11.7

Table S6. Device performance of flexible LEDs at various luminances. The table summarizes the voltage applied, EQE, current efficiency, and luminous power efficiency at 100 and 1000 cd m^{-2} as shown in Fig. S10. The emissive layer is the perovskite nanocrystals synthesized with OA:PbBr$_2$ of 4:1.

N_{th} device	Voltage [V]		EQE [%]		Current Efficiency [cd A^{-1}]		Luminous Power Efficiency [lm W^{-1}]	
	@ 100 cd m^{-2}	@ 1000 cd m^{-2}	@ 100 cd m^{-2}	@ 1000 cd m^{-2}	@ 100 cd m^{-2}	@ 1000 cd m^{-2}	@ 100 cd m^{-2}	@ 1000 cd m^{-2}
1	2.9	3.7	7.6	10.4	33.2	45.3	36.0	38.4
2	2.9	3.7	7.7	9.5	33.6	41.6	36.5	35.3
3	2.9	3.7	8.9	10.9	38.5	47.2	41.7	40.1
4	2.9	3.6	8.0	10.9	35.2	47.6	38.1	41.5
5	2.8	3.4	8.5	11.7	37.2	51.0	41.7	47.1
6	2.9	3.6	8.2	11.3	35.6	49.3	38.5	43.0

Table S7. Table summarizes the device characteristics of large area LED devices as shown in Fig. S11. At maximum luminance, LEDs with area > 15.2 mm^2 saturated the spectrometer. The bracketed number showed the characteristic values after corrected for the saturation, by scaling the luminance values linearly according to the spectral regions that does not saturate the spectrometer with the assumption that the spectral shape does not change at any injection density. Note: the largest area device (95.2 mm^2) is larger than the opening of the integrating sphere (78.5 mm^2). The reported values are not corrected for the loss of photons (i.e. the photons not collected by the integrating sphere). The emissive layer is the perovskite nanocrystals synthesized with OA:$PbBr_2$ of 4:1.

Device Area [mm^{-2}]	Luminance [cd m^{-2}]	Current Efficiency [cd A^{-1}]	Luminous Power Efficiency [lm W^{-1}]	EQE [%]
8.97	20577	42.7	39.2	9.9
15.2	19688 (22332)	37.2	34.2	8.6
35.4	12438 (20016)	30.9	24.3	7.2
95.2	6106 (13658)	22.8 (24.5)	18.7	5.3 (5.7)

Table S8. Device performance of large area LEDs at various luminances as shown in Fig. S11. The table summarizes the voltage applied, EQE, current efficiency, and luminous power efficiency at 100 and 1000 cd m^{-2}.

Device Area [mm^2]	Voltage [V]		EQE [%]		Current Efficiency [cd A^{-1}]		Luminous Power Efficiency [lm W^{-1}]	
	@ 100 cd m^{-2}	@ 1000 cd m^{-2}	@ 100 cd m^{-2}	@ 1000 cd m^{-2}	@ 100 cd m^{-2}	@ 1000 cd m^{-2}	@ 100 cd m^{-2}	@ 1000 cd m^{-2}
8.97	2.7	3.2	5.8	9.2	25.3	39.9	29.4	39.2
15.2	2.7	3.2	5.1	8.1	21.9	34.9	25.5	34.2
35.4	2.9	3.9	3.3	6.1	14.4	26.1	15.6	21.0
95.2	3.4	3.9	3.2	5.3	13.8	22.8	12.8	18.4

Table S9. Tabulated decay times for the global fitting result shown in Fig. S21.

	OA:$PbBr_2$ [-]				
	3:1#	4:1#	5:1*	7:1#	10:1*
t_1 [ps]	0.34 ± 0.01	0.11 ± 0.01	0.25 ± 0.01	0.11 ± 0.003	0.15 ± 0.01
t_2 [ps]	6.80 ± 0.11	5.73 ± 0.13	5.83 ± 0.08	2.60 ± 0.04	4.287 ± 0.05
t_3 [ps]	46.56 ± 1.36	33.71 ± 3.24	42.58 ± 0.31	24.91 ± 0.36	36.78 ± 2.27
t_4 [ps]	949.5 ± 23.1	719.3 ± 14.4	742.7 ± 5.6	628.6 ± 18.2	804.6 ± 18.6

Averaged 6 times

* Averaged 18 times

Table S10. Characteristic fluorescence lifetimes for OA:$PbBr_2$ = 3:1, after 405 nm excitation and signal collection at different emission wavelengths as shown in Fig. S23(a).

Emission Wavelength [nm]	A_1 [-]	τ_1 [ns]	A_2 [-]	τ_2 [ns]	τ_{av} [ns]
440	0.79	0.8	0.21	7.0	2.1
460	0.71	1.4	0.29	9.3	3.7
480	0.71	1.5	0.29	8.9	3.7
500	0.72	1.7	0.28	11.3	4.3
520	0.61	2.6	0.39	20.8	9.6
540	0.52	3.2	0.48	27.7	15.1

Table S11. Characteristic fluorescence lifetimes for OA:$PbBr_2$ = 4:1, after 405 nm excitation and signal collection at different emission wavelengths as shown in Fig. S23(b).

Emission Wavelength [nm]	A_1 [-]	τ_1 [ns]	A_2 [-]	τ_2 [ns]	τ_{av} [ns]
440	0.79	1.0	0.21	7.8	2.4
460	0.74	1.3	0.26	8.9	3.3
480	0.72	1.6	0.28	10.0	3.9
500	0.65	1.9	0.35	12.5	5.6
520	0.63	2.5	0.37	17.6	8.1
540	0.52	3.1	0.48	23.9	13.2

Table S12. Characteristic fluorescence lifetimes for OA:$PbBr_2$ = 5:1, after 405 nm excitation and signal collection at different emission wavelengths as shown in Fig. 6(b).

Emission Wavelength [nm]	A_1 [-]	τ_1 [ns]	A_2 [-]	τ_2 [ns]	τ_{av} [ns]
440	0.95	0.6	0.05	4.4	0.8
460	0.60	1.3	0.40	8.7	4.3
480	0.58	1.7	0.42	9.5	4.9
500	0.56	2.3	0.44	11.2	6.2
520	0.52	4.3	0.48	16.8	10.3
540	0.42	4.3	0.58	18.1	12.1

Table S13. Characteristic fluorescence lifetimes for OA:$PbBr_2$ = 7:1, after 405 nm excitation and signal collection at different emission wavelengths as shown in Fig. S23(c).

Emission Wavelength	A_1	τ_1	A_2	τ_2	τ_{av}
[nm]	[-]	[ns]	[-]	[ns]	[ns]
440	0.84	0.7	0.16	5.6	1.5
460	0.72	1.5	0.28	9.5	3.7
480	0.65	1.7	0.35	10.0	4.6
500	0.64	2.3	0.36	9.9	5.0
520	0.64	2.3	0.36	13.2	6.2
540	0.50	16.3	0.50	4.1	10.2

Table S14. Characteristic fluorescence lifetimes for OA:$PbBr_2$ = 10:1, after 405 nm excitation and signal collection at different emission wavelengths as shown in Fig. S23(d).

Emission Wavelength	A_1	τ_1	A_2	τ_2	τ_{av}
[nm]	[-]	[ns]	[-]	[ns]	[ns]
440	0.95	0.5	0.05	5.3	0.7
460	0.90	0.5	0.10	7.2	1.2
480	0.89	0.6	0.11	8.7	1.5
500	0.67	1.0	0.33	8.2	3.3
520	0.51	4.3	0.49	18.6	11.3
540	0.48	4.2	0.52	21.9	13.4

References:

1. Y. Cao, I. D. Parker, G. Yu, C. Zhang and A. J. Heeger, *Nature*, 1999, **397**, 414-417.
2. X. Dai, Z. Zhang, Y. Jin, Y. Niu, H. Cao, X. Liang, L. Chen, J. Wang and X. Peng, *Nature*, 2014, **515**, 96-99.
3. B. R. Pauw, J. S. Pedersen, S. Tardif, M. Takata and B. B. Iversen, *J Appl Crystallogr*, 2013, **46**, 365-371.
4. G. Xing, B. Wu, X. Wu, M. Li, B. Du, Q. Wei, J. Guo, E. K. L. Yeow, T. C. Sum and W. Huang, *Nat. Commun.*, 2017, **8**, 14558.
5. M. E. F. Bouduban, A. Burgos-Caminal, R. Ossola, J. Teuscher and J.-E. Moser, *Chem Sci*, 2017, **8**, 4371-4380.
6. Y. Shirasaki, G. J. Supran, M. G. Bawendi and V. Bulović, *Nat. Photon.*, 2012, **7**, 13.
7. H. H. Chou and C. H. Cheng, *Adv. Mater.*, 2010, **22**, 2468-2471.
8. J. Kwak, W. K. Bae, D. Lee, I. Park, J. Lim, M. Park, H. Cho, H. Woo, D. Y. Yoon and K. Char, *Nano Lett.*, 2012, **12**, 2362-2366.
9. Y. H. Kim, H. Cho, J. H. Heo, T. S. Kim, N. Myoung, C. L. Lee, S. H. Im and T. W. Lee, *Adv. Mater.*, 2015, **27**, 1248-1254.
10. J. Wang, N. Wang, Y. Jin, J. Si, Z. K. Tan, H. Du, L. Cheng, X. Dai, S. Bai, H. He, Z. Ye, M. L. Lai, R. H. Friend and W. Huang, *Adv. Mater.*, 2015, **27**, 2311-2316.
11. S. G. Bade, J. Li, X. Shan, Y. Ling, Y. Tian, T. Dilbeck, T. Besara, T. Geske, H. Gao, B. Ma, K. Hanson, T. Siegrist, C. Xu and Z. Yu, *ACS Nano*, 2016, **10**, 1795-1801.
12. Y. K. Chih, J. C. Wang, R. T. Yang, C. C. Liu, Y. C. Chang, Y. S. Fu, W. C. Lai, P. Chen, T. C. Wen, Y. C. Huang, C. S. Tsao and T. F. Guo, *Adv. Mater.*, 2016, **28**, 8687-8694.
13. Y. Ling, Y. Tian, X. Wang, J. C. Wang, J. M. Knox, F. Perez-Orive, Y. Du, L. Tan, K. Hanson, B. Ma and H. Gao, *Adv. Mater.*, 2016, **28**, 8983–8989.
14. J. Li, X. Shan, S. G. R. Bade, T. Geske, Q. Jiang, X. Yang and Z. Yu, *J. Phys. Chem. Lett.*, 2016, **7**, 4059-4066.
15. J. Song, J. Li, X. Li, L. Xu, Y. Dong and H. Zeng, *Adv. Mater.*, 2015, **27**, 7162-7167.
16. G. Li, F. W. R. Rivarola, N. J. L. K. Davis, S. Bai, T. C. Jellicoe, F. de la Peña, S. Hou, C. Ducati, F. Gao, R. H. Friend, N. C. Greenham and Z.-K. Tan, *Adv. Mater.*, 2016, **28**, 3528-3534.
17. J. Xing, F. Yan, Y. Zhao, S. Chen, H. Yu, Q. Zhang, R. Zeng, H. V. Demir, X. Sun, A. Huan and Q. Xiong, *ACS Nano*, 2016, **10**, 6623-6630.
18. J. Li, L. Xu, T. Wang, J. Song, J. Chen, J. Xue, Y. Dong, B. Cai, Q. Shan, B. Han and H. Zeng, *Adv. Mater.*, 2017, **29**, 1603885.
19. S. Y. Kim, W. I. Jeong, C. Mayr, Y. S. Park, K. H. Kim, J. H. Lee, C. K. Moon, W. Brütting and J. J. Kim, *Adv. Funct. Mater.*, 2013, **23**, 3896-3900.
20. D. R. Lee, B. S. Kim, C. W. Lee, Y. Im, K. S. Yook, S.-H. Hwang and J. Y. Lee, *ACS Appl. Mater. & Interfaces*, 2015, **7**, 9625-9629.
21. C. Y. Kuei, W. L. Tsai, B. Tong, M. Jiao, W. K. Lee, Y. Chi, C. C. Wu, S. H. Liu, G. H. Lee and P. T. Chou, *Adv. Mater.*, 2016, **28**, 2795-2800.
22. Z. Yan, Y. Wang, J. Wang, Y. Wang, J. Ding and L. Wang, *J. Mater. Chem. C*, 2017, **5**, 10122-10125.

23. J. R. Manders, L. Qian, A. Titov, J. Hyvonen, J. Tokarz ‐ Scott, K. P. Acharya, Y. Yang, W. Cao, Y. Zheng and J. Xue, *J. Soc. Inf. Disp.*, 2015, **23**, 523-528.
24. H. Zhang, S. Chen and X. W. Sun, *ACS nano*, 2017.
25. Z.-K. Tan, R. S. Moghaddam, M. L. Lai, P. Docampo, R. Higler, F. Deschler, M. Price, A. Sadhanala, L. M. Pazos, D. Credgington, F. Hanusch, T. Bein, H. J. Snaith and R. H. Friend, *Nat. Nano.*, 2014, **9**, 687-692.
26. H. Cho, S.-H. Jeong, M.-H. Park, Y.-H. Kim, C. Wolf, C.-L. Lee, J. H. Heo, A. Sadhanala, N. Myoung, S. Yoo, S. H. Im, R. H. Friend and T.-W. Lee, *Science*, 2015, **350**, 1222-1225.
27. Z. Xiao, R. A. Kerner, L. Zhao, N. L. Tran, K. M. Lee, T.-W. Koh, G. D. Scholes and B. P. Rand, *Nat. Photon.*, 2017, **11**, 108.
28. J. Pan, L. N. Quan, Y. Zhao, W. Peng, B. Murali, S. P. Sarmah, M. Yuan, L. Sinatra, N. M. Alyami, J. Liu, E. Yassitepe, Z. Yang, O. Voznyy, R. Comin, M. N. Hedhili, O. F. Mohammed, Z. H. Lu, D. H. Kim, E. H. Sargent and O. M. Bakr, *Adv. Mater.*, 2016, **28**, 8718-8725.
29. K. Okumoto, H. Kanno, Y. Hamaa, H. Takahashi and K. Shibata, *Appl. Phys. Lett.*, 2006, **89**, 063504.
30. W. K. Bae, J. Kwak, J. W. Park, K. Char, C. Lee and S. Lee, *Adv. Mater.*, 2009, **21**, 1690-1694.
31. K.-H. Lee, J.-H. Lee, H.-D. Kang, B. Park, Y. Kwon, H. Ko, C. Lee, J. Lee and H. Yang, *ACS Nano*, 2014, **8**, 4893-4901.
32. H. P. Kim, J. Kim, B. S. Kim, H.-M. Kim, J. Kim, A. R. b. M. Yusoff, J. Jang and M. K. Nazeeruddin, *Adv. Opt. Mater.*, 2017, **5**, 1600920.
33. J.-W. Lee, Y. J. Choi, J.-M. Yang, S. Ham, S. K. Jeon, J. Y. Lee, Y.-H. Song, E. K. Ji, D.-H. Yoon, S. Seo, H. Shin, G. S. Han, H. S. Jung, D. Kim and N.-G. Park, *ACS Nano*, 2017, **11**, 3311-3319.
34. Y.-H. Kim, C. Wolf, Y.-T. Kim, H. Cho, W. Kwon, S. Do, A. Sadhanala, C. G. Park, S.-W. Rhee, S. H. Im, R. H. Friend and T.-W. Lee, *ACS Nano*, 2017, **11**, 6586-6593.
35. L. Zhang, X. Yang, Q. Jiang, P. Wang, Z. Yin, X. Zhang, H. Tan, Y. Yang, M. Wei, B. R. Sutherland, E. H. Sargent and J. You, *Nat. Commun.*, 2017, **8**, 15640.
36. N. Stribeck, *X-ray scattering of soft matter*, Springer Science & Business Media, 2007.
37. O. Glatter and O. Kratky, *Small angle X-ray scattering*, Academic press, 1982.
38. A. Guiner, G. Fournet and C. Walker, *J. Wiley & Sons, New York*, 1955.
39. R. L. Z. Hoye, M. R. Chua, K. P. Musselman, G. Li, M.-L. Lai, Z.-K. Tan, N. C. Greenham, J. L. MacManus-Driscoll, R. H. Friend and D. Credgington, *Adv. Mater.*, 2015, **27**, 1414-1419.
40. G. Li, Z.-K. Tan, D. Di, M. L. Lai, L. Jiang, J. H.-W. Lim, R. H. Friend and N. C. Greenham, *Nano Lett.*, 2015, **15**, 2640-2644.
41. J. C. Yu, D. B. Kim, E. D. Jung, B. R. Lee and M. H. Song, *Nanoscale*, 2016, **8**, 7036-7042.
42. Y. Ling, Z. Yuan, Y. Tian, X. Wang, J. C. Wang, Y. Xin, K. Hanson, B. Ma and H. Gao, *Adv. Mater.*, 2016, **28**, 305-311.
43. L. Meng, E.-P. Yao, Z. Hong, H. Chen, P. Sun, Z. Yang, G. Li and Y. Yang, *Adv. Mater.*, 2017, **29**, 1603826.

44. A. Perumal, S. Shendre, M. Li, Y. K. E. Tay, V. K. Sharma, S. Chen, Z. Wei, Q. Liu, Y. Gao, P. J. S. Buenconsejo, S. T. Tan, C. L. Gan, Q. Xiong, T. C. Sum and H. V. Demir, *Sci. Rep.*, 2016, **6**, 36733.
45. C. Wu, Y. Zou, T. Wu, M. Ban, V. Pecunia, Y. Han, Q. Liu, T. Song, S. Duhm and B. Sun, *Adv. Funct. Mater.*, 2017, **27**, 1700338.
46. Y.-H. Kim, G.-H. Lee, Y.-T. Kim, C. Wolf, H. J. Yun, W. Kwon, C. G. Park and T. W. Lee, *Nano Energy*, 2017, **38**, 51-58.
47. S. Kumar, J. Jagielski, N. Kallikounis, Y.-H. Kim, C. Wolf, F. Jenny, T. Tian, C. J. Hofer, Y.-C. Chiu, W. J. Stark, T.-W. Lee and C.-J. Shih, *Nano Lett.*, 2017, **17**, 5277-5284.